Gamma rays and gravitational waves from inelastic Higgs portal dark matter

Dan Hooper,[1,2,*] Gordan Krnjaic,[3,4,5,†] Duncan Rocha,[3,6,‡] and Subhojit Roy[7,§]

[1]*Department of Physics, University of Wisconsin, Madison, Wisconsin, USA*
[2]*Wisconsin IceCube Particle Astrophysics Center, University of Wisconsin, Madison, Wisconsin, USA*
[3]*Theoretical Physics Division, Fermi National Accelerator Laboratory, Batavia, Illinois, USA*
[4]*Department of Astronomy and Astrophysics, University of Chicago, Chicago, Illinois, USA*
[5]*Kavli Institute for Cosmological Physics, University of Chicago, Chicago, Illinois, USA*
[6]*Department of Physics, University of Chicago, Chicago, Illinois, USA*
[7]*High-Energy Physics Division, Argonne National Laboratory, Argonne, Illinois, USA*

(Received 14 August 2025; accepted 13 May 2026; published 3 June 2026)

We explore a simple and predictive dark matter scenario involving a *complex* scalar field, ϕ, coupled to the Higgs portal with no additional field content. In the UV, the field possesses a global $U(1)$ symmetry which is broken by mass terms and Higgs portal interactions. In the mass basis, the complex field splits into a pair of real scalars with a small mass splitting (in analogy to pseudo-Dirac fermions), such that the Higgs portal acquires both diagonal and off-diagonal terms with respect to these eigenstates. In the parameter space where the off-diagonal interaction predominates, this scenario is safe from direct detection constraints. Moreover, this model provides a viable explanation for the longstanding Galactic Center γ-ray excess. Additionally, this model influences the Higgs potential in a way that could facilitate a strong first-order electroweak phase transition in the early Universe, potentially leading to a stochastic gravitational wave background that could fall within the reach of upcoming space-based detectors.

DOI: 10.1103/4vqv-vmxz

I. INTRODUCTION

One of the simplest and most predictive dark matter (DM) models involves a singlet scalar field coupled to the Higgs portal [1–10],

$$\mathcal{L} \supset -\frac{1}{2}(m_\phi^2 + kH^\dagger H)\phi^2, \tag{1}$$

where ϕ is a real scalar that is stabilized by a Z_2 symmetry, H is the Standard Model (SM) Higgs doublet, and κ is the strength of the portal coupling. If k is sufficiently large, the ϕ population will thermalize with the Standard Model bath in the early Universe and then freeze out of chemical equilibrium, leaving behind a thermal relic abundance.

If $m_\phi \gg m_h$, DM annihilation can proceed in this model through $\phi\phi \to h \to W^+W^-$, $\phi\phi \to h \to ZZ$, and $\phi\phi \to hh$, collectively leading to the following thermal relic abundance [7]:

$$\Omega_\phi h^2 \approx \Omega_{\rm DM} h^2 \left(\frac{0.15}{k}\right)^2 \left(\frac{m_\phi}{\rm TeV}\right)^2, \tag{2}$$

where $\Omega_{\rm DM}h^2 \approx 0.12$ is the measured DM abundance [11]. In the opposite regime, $m_\phi \lesssim m_h$, the dominant annihilation channels proceed through s-channel Higgs exchange to Standard Model fermions or gauge bosons.

For each choice of the DM mass in this scenario, there is a unique value of k that yields the measured DM abundance. This value of k, in turn, determines the magnitude of the signals that are predicted at direct and indirect detection experiments, as well as at colliders. With the exception of the region near the Higgs resonance, $m_\phi \approx m_h/2$, where an acceptable relic abundance can be achieved for small values of k, this model is ruled out by a combination of direct detection [12–14], indirect detection [15], and collider constraints [16–18].

In this paper, we investigate a scenario in which the Higgs portal DM candidate, ϕ, is promoted to a *complex* scalar field. If all allowed mass terms are present, the complex field splits into a pair of nondegenerate mass eigenstates, $\phi_{1,2}$. For some choices of the masses and couplings, the dominant Higgs portal interaction is off-diagonal in the mass basis,

*Contact author: dwhooper@wisc.edu
†Contact author: krnjaicg@fnal.gov
‡Contact author: drocha@uchicago.edu
§Contact author: sroy@anl.gov

Published by the American Physical Society under the terms of the Creative Commons Attribution 4.0 International license. Further distribution of this work must maintain attribution to the author(s) and the published article's title, journal citation, and DOI. Funded by SCOAP³.

$$\mathcal{L} \supset g\phi_1\phi_2 H^\dagger H, \tag{3}$$

where g is a dimensionless coupling. This operator leads to *inelastic* scattering at direct detection experiments, greatly weakening constraints from nuclear recoil searches.

The inelastic scalar Higgs portal DM scenario has been previously explored in Refs. [13,14,19–21]. In this work, we revisit this model's predictions in light of recent constraints from direct detection experiments. We further examine the ability of this scenario to explain the spectrum, angular distribution, and overall intensity of the observed excess of GeV-scale emission from the Galactic Center [22–24], as well as the excess of ∼10–20 GeV antiprotons in the cosmic-ray spectrum [25–27].

In order for the matter-antimatter asymmetry of our Universe to have been generated through electroweak baryogenesis [28–31], there must have been a strong first-order phase transition in the Higgs field. This can be achieved by introducing extra scalar degrees of freedom which modify the Higgs potential. In this work, we show that the inclusion of the complex scalar field, ϕ, can significantly impact the shape of the Higgs potential, allowing for a strong first-order phrase transition. Such a phase transition would generate a stochastic background gravitational waves [32] that could potentially be detectable by future space-based gravitational wave observatories.

The remainder of this paper is organized as follows: in Sec. II, we discuss the theoretical framework of the inelastic Higgs portal model. In Secs. III and IV, we consider the constraints from direct detection experiments and calculate the thermal relic abundance of DM in this model. In Secs. V and VI, we consider the cosmological constraints on this model and discuss its ability to produce a signal that is consistent with the Galactic Center γ-ray excess. The electroweak phase transition (EWPT) and the production of gravitational waves in this model are described in Secs. VII–IX. Collider probes of the relevant parameter space in this model are discussed in Sec. X. We summarize our results and present our conclusions in Sec. XI. In a series of Appendixes, we discuss contributions to the DM's elastic scattering cross section at one-loop level, the Higgs potential at finite temperature, and the production of gravitational waves from a first-order phase transition in the early Universe.

II. MODEL OVERVIEW

The tree-level Standard Model Higgs potential can be expressed as follows:

$$V_{\rm SM} = -\mu_h^2 H^\dagger H + \lambda_h (H^\dagger H)^2, \tag{4}$$

where H is the Standard Model Higgs doublet. In our scenario, we introduce a complex scalar field, ϕ, with fully general mass terms. Prior to electroweak symmetry breaking, the Lagrangian includes the following terms:

$$\mathcal{L}_m = -m_0^2|\phi|^2 - \frac{1}{2}(\rho_0^2\phi^2 + \rho_0^{*2}\phi^{*2}), \tag{5}$$

where m_0 is a real mass parameter, ρ_0 is a complex dimensionful scale, and there is a Z_2 symmetry under which $\phi \to -\phi$. We also include corresponding bilinear Higgs portal couplings,

$$\mathcal{L}_{\phi h} = -\left[\kappa|\phi|^2 + \frac{1}{2}(\eta\phi^2 + \eta^*\phi^{*2})\right] H^\dagger H, \tag{6}$$

where κ is a real coupling, and η is a complex coupling. In addition to the mass terms and Higgs portal interactions, the most general renormalizable scalar potential also contains quartic self-interactions of the singlet fields, which will play an important role in determining the early Universe phase transition dynamics. For clarity, we defer the full expression of these terms to Sec. VII, where we analyze the electroweak phase transition in detail. After electroweak symmetry breaking, the mass terms from Eq. (5) become

$$\mathcal{L}_m \to -m^2|\phi|^2 - \frac{1}{2}(\rho^2\phi^2 + \rho^{*2}\phi^{*2}), \tag{7}$$

where we have defined the parameters

$$m^2 \equiv m_0^2 + \frac{\kappa v_h^2}{2}, \qquad \rho^2 \equiv \rho_0^2 + \frac{\eta v_h^2}{2}, \tag{8}$$

which include contributions from electroweak symmetry breaking, and where $v_h \approx 246$ GeV is the vacuum expectation value (VEV) of the Higgs field. This set of mass terms and Higgs portal interactions can arise if ϕ enjoys an approximate $U(1)$ global symmetry under which $\phi \to e^{i\theta}\phi$. We assume this symmetry is broken only by the ϕ^2 terms in the Lagrangian, and prohibit linear ϕ interactions that would induce DM decay.[1]

After diagonalizing the mass matrix in Eq. (5), the mass eigenstates of the theory are ϕ_1 and ϕ_2, with corresponding eigenvalues that are given by

$$m^2_{\phi_1,\phi_2} = m^2 \mp |\rho^2|. \tag{9}$$

In the limit of a small mass splitting, we have

$$\Delta m = m_{\phi_2} - m_{\phi_1} \approx \frac{|\rho^2|}{m}. \tag{10}$$

The fields in the interaction basis can be written as

[1]Avoiding linear interactions can be achieved if, for example, the complex field, ϕ, has a charge of +1 under the $U(1)$ and our desired breaking terms arise from the VEV of an additional scalar, Φ, with a charge of +2. This allows terms of the form $\Phi\phi^2 \to \langle\Phi\rangle\phi^2$ to arise without generating any terms that are linear in ϕ because, when Φ acquires a VEV, there is a residual Z_2 symmetry under which the real mass eigenstates transform as $\phi_i \to -\phi_i$.

$$\phi = \alpha\phi_1 + \beta\phi_2, \qquad \phi^* = \alpha^*\phi_1 + \beta^*\phi_2, \tag{11}$$

where $\alpha = e^{-i\theta}/\sqrt{2}$, $\beta = ie^{-i\theta}/\sqrt{2}$, and θ is the angle that diagonalizes the matrix associated with Eq. (7), as follows:

$$\mathcal{U} = \begin{pmatrix} \cos\theta & -\sin\theta \\ \sin\theta & \cos\theta \end{pmatrix}, \tag{12}$$

where $\cos 2\theta = \mathrm{Re}(\rho^2)/|\rho^2|$ and $\sin 2\theta = \mathrm{Im}(\rho^2)/|\rho^2|$.

After electroweak symmetry breaking, the Higgs portal interactions given in Eq. (6), written in the mass basis, become

$$\mathcal{L}_{\phi h} = -(f_1\phi_1^2 + f_2\phi_2^2 + g\phi_1\phi_2)\left(-v_h h + \frac{h^2}{2}\right), \tag{13}$$

where we have defined the diagonal (elastic) couplings,

$$\begin{aligned} f_1 &= \frac{\kappa}{2} + \frac{1}{2}(\eta\alpha^2 + \eta^*\alpha^{*2}) \\ &= \frac{\kappa}{2} + \frac{1}{2}\mathrm{Re}(\eta)\cos 2\theta + \frac{1}{2}\mathrm{Im}(\eta)\sin 2\theta, \end{aligned} \tag{14}$$

$$\begin{aligned} f_2 &= \frac{\kappa}{2} + \frac{1}{2}(\eta\beta^2 + \eta^*\beta^{*2}) \\ &= \frac{\kappa}{2} - \frac{1}{2}\mathrm{Re}(\eta)\cos 2\theta - \frac{1}{2}\mathrm{Im}(\eta)\sin 2\theta, \end{aligned} \tag{15}$$

and the off-diagonal (inelastic) coupling,

$$g = \eta\alpha\beta + \eta^\star\alpha^\star\beta^\star = \mathrm{Re}(\eta)\sin 2\theta - \mathrm{Im}(\eta)\cos 2\theta. \tag{16}$$

In regions of parameter space with $|f_1| \ll |g|, |f_2|$, this model deviates qualitatively from the familiar case of DM in the form of a real scalar that couples to the Standard Model through the Higgs portal.

III. DIRECT DETECTION

In the traditional Higgs portal scenario characterized by Eq. (1), the DM is a real scalar which undergoes efficient elastic scattering with nuclei. For values of the portal coupling, κ, that give rise to the observed relic density, this elastic scattering cross section is excluded by existing direct detection experiments [33], except in the fine-tuned Higgs resonance window near $m_\phi \approx m_h/2$.

By contrast, in our version of the Higgs portal scenario, the DM can scatter elastically ($\phi_1 N \to \phi_1 N$) through the coupling, f_1, or inelastically ($\phi_1 N \to \phi_2 N$) through the coupling, g. The latter process is only possible if the mass splitting between the two states satisfies the inequality [34]

$$\Delta m < \frac{\mu_{\phi_1 N}}{2} v^2, \tag{17}$$

where v is the velocity of the DM particle and $\mu_{\phi_1 N}$ is the reduced mass of the DM-nucleus system. For the case of a xenon target and $v \sim 300$ km/s, inelastic scattering can occur only if $\Delta m \lesssim 50$ keV. Throughout this study, we will restrict ourselves to the parameter space in which $\Delta m \gtrsim$ MeV, for which inelastic scattering will be prohibitively suppressed.

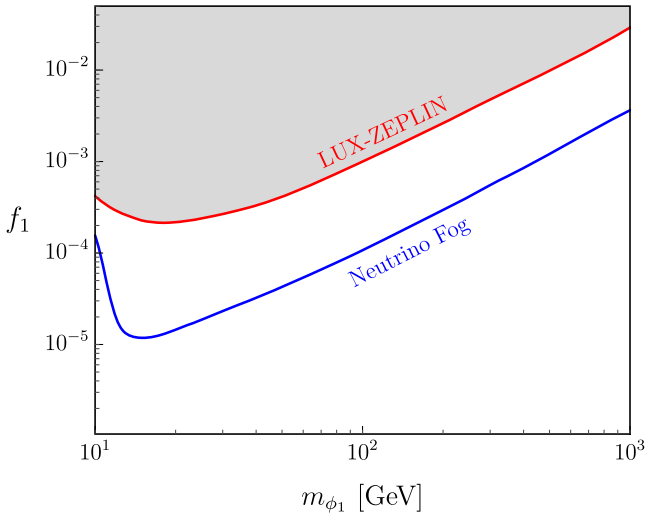


FIG. 1. Maximum value of f_1 consistent with constraints from the LZ experiment [33]. Also shown is the value of this parameter that would lead to an elastic scattering cross section at the boundary of the so-called "neutrino fog" [38].

In this scenario, the spin-independent cross section for elastic scattering off nuclei can be written as

$$\begin{aligned} \sigma^{\mathrm{SI}}_{\phi_1 N} &= \frac{f_1^2 m_N^2 \mu^2_{\phi_1 N}}{\pi m_{\phi_1}^2 m_h^4}\left(\sum_{q=u,d,s} f^N_{T_q} + \frac{2}{27}\sum_{q=c,b,t} f^N_{\mathrm{TG}}\right)^2 \\ &\approx 4\times 10^{-46}\ \mathrm{cm}^2\left(\frac{f_1}{0.1}\right)^2\left(\frac{\mathrm{TeV}}{m_{\phi_1}}\right)^2, \end{aligned} \tag{18}$$

where $N = p, n$, $\mu_{\phi_1 N}$ is the $\phi_1 - N$ reduced mass, and the terms in the sums are nuclear matrix elements. Here, $f^N_{T_q}$ denotes the nucleon matrix elements of the light quark scalar operators, defined by $m_N f^N_{T_q} \equiv \langle N|m_q\bar{q}q|N\rangle$, while $f^N_{\mathrm{TG}} = 1 - \sum_{q=u,d,s} f^N_{T_q}$ accounts for the gluon contribution via the trace anomaly.[2] The null results of direct detection experiments allow us to place stringent constraints on the coupling, f_1, and thus require $|f_1| \ll |g|$ to obtain an acceptable thermal relic abundance. In Fig. 1, we show the maximum value of $|f_1|$ that is consistent with the recent limits placed by the LUX-ZEPLIN (LZ) Collaboration [33], as a function of m_{ϕ_1}. This constraint meaningfully impacts the regions of parameter space that are potentially viable within this model. In this analysis, we

[2]From Ref. [35], we take $f^p_{T_u} = 0.018$, $f^p_{T_d} = 0.027$, $f^p_{T_s} = 0.037$, $f^n_{T_u} = 0.013$, $f^n_{T_d} = 0.040$, $f^n_{T_s} = 0.037$, and $f^{p,n}_{\mathrm{TG}} = 0.91$.

TABLE I. Parameters for two selected benchmark models (BP1 and BP2), along with the masses of the dark matter and its excited state, the dark matter's thermal relic abundance, and the cross sections relevant for direct and indirect detection.

Input/Observables	BP1	BP2
λ_1	0.4	1.6
λ_2	0.4	1.3
λ_{12}	0.3	0.2
f_1	0.0004	0.0009
f_2	0.26	0.49
g	0.046	0.16
m_{ϕ_1} (GeV)	68.7	130
m_{ϕ_2} (GeV)	71.4	150
$\Omega_{\phi_1} h^2$	0.12	0.12
$\sigma^{\rm SI}_{\phi_1 N}$ (cm^2)	1.4×10^{-48}	1.8×10^{-48}
$\langle\sigma v\rangle_{\phi_1\phi_1}$ (cm^3/s)	4.9×10^{-30}	1.6×10^{-26}

have used the publicly available package, FeynRules [36], which we interface with MicrOMEGAs [37] to obtain the DM relic abundance, as well as the cross sections relevant for direct and indirect searches.

For completeness, we note that there are one-loop contributions to the $\phi_1 N \to \phi_1 N$ elastic scattering cross section which depend on g and f_2, rather than f_1. The corresponding Feynman diagrams involve a vertex correction to the $\phi_1\phi_1 h$ interaction induced by three propagators from virtual ϕ_2 and h internal lines (see Appendix A). For the benchmark models presented in Table I, we have verified that these contributions are subdominant. We also note that direct detection signals could be enhanced in this model if the coefficient of the $\lambda_{12}\phi_1^2\phi_2^2$ quartic operator is large. This coupling primarily impacts the EWPT and the corresponding gravitational wave signal (see Sec. VII), and does not play a significant role in determining the DM relic density.

IV. THERMAL RELIC ABUNDANCE

In the early Universe, $T \gg m_{\phi_1}, m_{\phi_2}$, and the ϕ_1 and ϕ_2 populations were each maintained in chemical equilibrium with the Standard Model radiation bath. As the Universe expanded and cooled, these species froze out of chemical equilibrium, leaving behind a thermal relic abundance. In the case of $\Delta m \ll T_{\rm FO} \approx m_{\phi_1}/20$, the mass splitting between these two states was negligible during the process of thermal freeze-out, allowing both annihilations and coannihilations to deplete the abundances of these particles. For larger mass splittings, the thermal relic abundance is largely determined by rate of ϕ_1 annihilations.

In this scenario, the ϕ_1 population evolves according to the Boltzmann equation,

$$\dot{n}_{\phi_1} = -3Hn_{\phi_1} - \langle\sigma v\rangle_{\phi_1\phi_1}\left[n_{\phi_1}^2 - (n_{\phi_1}^{\rm eq})^2\right] - \langle\sigma v\rangle_{\phi_1\phi_2}\left[n_{\phi_1}n_{\phi_2} - n_{\phi_1}^{\rm eq}n_{\phi_2}^{\rm eq}\right], \quad (19)$$

and the ϕ_2 abundance evolves according to

$$\dot{n}_{\phi_2} = -3Hn_{\phi_2} - \langle\sigma v\rangle_{\phi_2\phi_2}\left[n_{\phi_2}^2 - (n_{\phi_2}^{\rm eq})^2\right] - \langle\sigma v\rangle_{\phi_1\phi_2}\left[n_{\phi_1}n_{\phi_2} - n_{\phi_1}^{\rm eq}n_{\phi_2}^{\rm eq}\right], \quad (20)$$

where the "eq" superscript denotes an equilibrium quantity, H is the Hubble rate, and the cross sections are thermally averaged and summed over all Standard Model final states. Since processes converting $\phi_1 \leftrightarrow \phi_2$ are efficient during this time, the quantities $n_{\phi_1}/(n_{\phi_1}+n_{\phi_2})$ and $n_{\phi_2}/(n_{\phi_1}+n_{\phi_2})$ remain near their equilibrium values throughout thermal freeze-out, allowing these Boltzmann equations to reduce to

$$\dot{n}_{\rm tot} = -3Hn_{\rm tot} - \langle\sigma v\rangle_{\rm eff}[n_{\rm tot}^2 - (n_{\rm tot}^{\rm eq})^2], \quad (21)$$

where $n_{\rm tot} \equiv n_{\phi_1} + n_{\phi_2}$, and the effective annihilation cross section is given by

$$\langle\sigma v\rangle_{\rm eff} = \frac{\langle\sigma v\rangle_{\phi_1\phi_1} + \epsilon^2\langle\sigma v\rangle_{\phi_2\phi_2} + 2\epsilon\langle\sigma v\rangle_{\phi_1\phi_2}}{(1+\epsilon)^2}, \quad (22)$$

where we have defined the parameter

$$\epsilon \equiv \frac{n_{\phi_2}^{\rm eq}}{n_{\phi_1}^{\rm eq}} = \left(1 + \frac{\Delta m}{m_{\phi_1}}\right)^{3/2} e^{-\Delta m/T}. \quad (23)$$

Each term in Eq. (22) is shorthand for a total annihilation/coannihilation cross section into all kinematically accessible Standard Model final states, as follows:

$$\langle\sigma v\rangle_{\phi_i\phi_j} \equiv \langle\sigma v\rangle_{\phi_i\phi_j\to WW} + \langle\sigma v\rangle_{\phi_i\phi_j\to ZZ} + \langle\sigma v\rangle_{\phi_i\phi_j\to hh} + \sum_f \langle\sigma v\rangle_{\phi_i\phi_j\to f\bar{f}}. \quad (24)$$

In the limit of a small mass splitting, the effective cross section reduces to

$$\langle\sigma v\rangle_{\rm eff} \approx \frac{1}{2}\langle\sigma v\rangle_{\phi_1\phi_2} + \frac{1}{4}(\langle\sigma v\rangle_{\phi_1\phi_1} + \langle\sigma v\rangle_{\phi_2\phi_2}). \quad (25)$$

Under the assumption of a negligible mass splitting, $m_{\phi_1} = m_{\phi_2} \equiv m_\phi$, the annihilation and coannihilation cross sections to fermionic final states are given by

$$\sigma_{\phi_i\phi_i\to f\bar{f}} = \frac{n_c f_i^2}{2\pi s}\sqrt{\frac{s-4m_f^2}{s-4m_\phi^2}}\left[\frac{m_f^2(s-4m_f^2)}{(s-m_h^2)^2 + m_h^2\Gamma_h^2}\right], \quad (26)$$

$$\sigma_{\phi_1\phi_2\to f\bar{f}} = \frac{n_c g^2}{8\pi s}\sqrt{\frac{s-4m_f^2}{s-4m_\phi^2}}\left[\frac{m_f^2(s-4m_f^2)}{(s-m_h^2)^2+m_h^2\Gamma_h^2}\right], \quad (27)$$

where $i = 1, 2$ and $n_c = 1(3)$ is the number of colors of the final state lepton (quark). If $m_\phi > m_h$, annihilations and coannihilations can also proceed through t-channel ϕ exchange and through a $\phi\phi hh$ vertex, resulting in the following cross sections, also given in the limit of equal ϕ_1 and ϕ_2 masses:

$$\sigma_{\phi_i\phi_i\to hh} = \frac{1}{8\pi s}\sqrt{\frac{s-4m_h^2}{s-4m_\phi^2}}\left[f_i^2 w(s)^2 + \frac{2(g^2+4f_i^2)^2 v_h^4}{A^2-B^2} + \frac{(g^2+4f_i^2)v_h^2}{AB}[(g^2+4f_i^2)v_h^2 - 2f_i A w(s)] \times \ln\left(\frac{A+B}{A-B}\right)\right], \quad (28)$$

$$\sigma_{\phi_1\phi_2\to hh} = \frac{g^2}{32\pi s}\sqrt{\frac{s-4m_h^2}{s-4m_\phi^2}}\left[w(s)^2 + \frac{32(f_1+f_2)^2 v_h^4}{A^2-B^2} + \frac{8(f_1+f_2)v_h^2}{AB}[2(f_1+f_2)v_h^2 - A w(s)] \times \ln\left(\frac{A+B}{A-B}\right)\right], \quad (29)$$

where $w(s) = (1+2m_h^2/s)/(1-m_h^2/s)$. Additionally, we have defined

$$A \equiv s - 2m_h^2, \quad B \equiv \sqrt{(s-4m_\phi^2)(s-4m_h^2)}. \quad (30)$$

Lastly, in the region in which $m_{W/Z} < m_{\phi_i} < m_h$, annihilations to W and Z bosons can be the dominant reaction. In the limit of equal scalar masses, the coannihilation cross sections to a pair of gauge bosons are given by

$$\sigma_{\phi_1\phi_2\to WW} = \frac{g^2}{16\pi s}\sqrt{\frac{s-4m_W^2}{s-4m_\phi^2}}\frac{8m_W^4+(s-2m_W^2)^2}{(s-m_h^2)^2+m_h^2\Gamma_h^2}, \quad (31)$$

$$\sigma_{\phi_1\phi_2\to ZZ} = \frac{g^2}{32\pi s}\sqrt{\frac{s-4m_Z^2}{s-4m_\phi^2}}\frac{8m_Z^4+(s-2m_Z^2)^2}{(s-m_h^2)^2+m_h^2\Gamma_h^2}. \quad (32)$$

The cross sections for $\phi_i\phi_i \to WW/ZZ$ can be computed by replacing $g \to 2f_i$ in the above equations.

From the cross sections given above, we can calculate the thermally averaged value following the standard procedure [39,40],

$$\langle\sigma v\rangle_{\phi_i\phi_j} = \frac{1}{N(T)}\int_{s_0}^{\infty} ds\,\sigma_{\phi_i\phi_j}\sqrt{s}(s-s_0)K_2\left(\frac{\sqrt{s}}{T}\right), \quad (33)$$

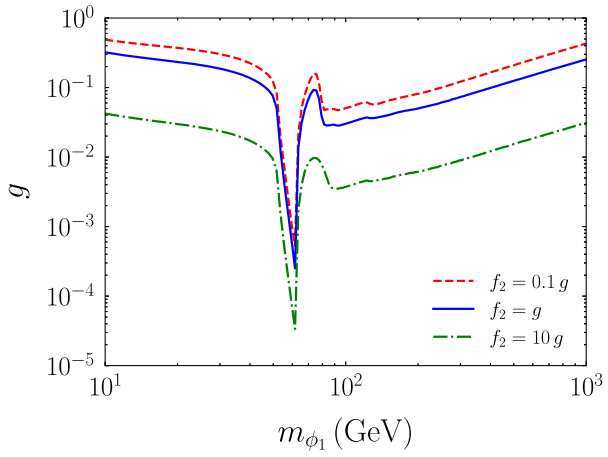


FIG. 2. Value of the coupling, g, that yields a thermal relic abundance of $\Omega_{\phi_1}h^2 = 0.12$, for $\Delta m = 0.1$ GeV and $f_1 = 0$. Results are shown for three values of f_2/g.

where $s_0 = (m_{\phi_i} + m_{\phi_j})^2$ is the centre-of-mass energy at zero momentum, $\sigma_{\phi_i\phi_j}$ is the total annihilation cross section to all Standard Model species, and

$$N(T) = 8m_{\phi_i}^2 m_{\phi_j}^2 T K_1\left(\frac{m_{\phi_i}}{T}\right)K_1\left(\frac{m_{\phi_j}}{T}\right), \quad (34)$$

is a normalization factor.

In Fig. 2, we present the value of the coupling, g, that is required to generate a thermal relic abundance of $\Omega_{\phi_1}h^2 = 0.12$, as a function of m_{ϕ_1}, and for $\Delta m = 0.1$ GeV and $f_1 = 0$. The results are shown for three different values of f_2/g. As the ratio f_2/g increases, the $\phi_2\phi_2$ annihilation cross section grows, necessitating a smaller value of g. In our regime of interest, $|g|, |f_2| \gg |f_1|$, a combination of coannihilations ($\phi_1\phi_2 \to hh$, $\phi_1\phi_2 \to f\bar{f}$), ϕ_2 annihilations ($\phi_2\phi_2 \to hh, \phi_2\phi_2 \to f\bar{f}$), and t-channel ϕ_1 annihilations ($\phi_1\phi_1 \to hh$) govern the relic abundance.

We are now in a position to comment on the degree of fine-tuning that is required in this model to be consistent with constraints from direct detection experiments. To obtain the required hierarchy, $|g|, |f_2| \gg |f_1|$, there must exist cancellations between the terms in Eq. (14). Comparing the values of f_2 and g that are required to obtain the desired thermal relic abundance to the upper limits on f_1 shown in Fig. 1, we find that these cancellations must occur at the roughly $\mathcal{O}(0.1\% - 10\%)$ level. For example, in the case of $g = f_2$, such cancellations would require $f_1/g \lesssim 10^{-3}$, 0.03, or 0.1, for $m_\phi = 10$ GeV, 100 GeV, or 1 TeV, respectively. Alternatively, instead of a cancellation between terms, this hierarchy of couplings could arise if all three of $\cos 2\theta$, $\mathrm{Im}(\eta)$, and κ are small (or if all three of $\sin 2\theta$, $\mathrm{Re}(\eta)$, and κ are small).

V. CONSTRAINTS FROM ϕ_2 DECAYS

In this model, ϕ_2 can decay into a ϕ_1 and Standard Model particles. These decays could impact the light element abundances or the ionization history of the Universe, leading to nontrivial cosmological constraints on the parameters of this model.

The process $\phi_2 \to \phi_1 \gamma\gamma$ can proceed through an off-shell Higgs boson, with contributions arising from the interaction term proportional to g in Eq. (13), in combination with the effective coupling of the Higgs boson to photons, represented by $(c_{\gamma\gamma} h/v_h) F_{\mu\nu} F^{\mu\nu}$, where $F_{\mu\nu}$ is the electromagnetic field strength tensor. The width for this process is given by

$$\Gamma_{\phi_2 \to \phi_1 \gamma\gamma} = \frac{g^2 c_{\gamma\gamma}^2 (\Delta m)^7}{210\pi^3 m_h^4 m_{\phi_2}^2} \approx 4 \times 10^{-22}\ \mathrm{s}^{-1} \left(\frac{g}{0.3}\right)^2 \left(\frac{\Delta m}{\mathrm{MeV}}\right)^7 \left(\frac{\mathrm{TeV}}{m_{\phi_2}}\right)^2, \quad (35)$$

where $c_{\gamma\gamma} \approx -2.03 \times 10^{-3}$ [41].

For $\Delta m > 2m_e$, decays to $\gamma\gamma$ are always subdominant to decays to fermions. In the $2m_f \ll \Delta m \ll m_{\phi_2}$ limit, the width for the process $\phi_2 \to \phi_1 f \bar{f}$ is given by

$$\Gamma_{\phi_2 \to \phi_1 f \bar{f}} = \frac{n_c g^2 m_f^2 (\Delta m)^5}{240\pi^3 m_h^4 m_{\phi_2}^2}, \quad (36)$$

where $n_c = 1(3)$ for decays to leptons (quarks). For $2m_e \ll \Delta m \ll 2m_\mu$, this yields

$$\Gamma_{\phi_2 \to \phi_1 ee} \approx 10^{-12}\ \mathrm{s}^{-1} \left(\frac{g}{0.2}\right)^2 \left(\frac{\Delta m}{10\ \mathrm{MeV}}\right)^5 \left(\frac{\mathrm{TeV}}{m_{\phi_2}}\right)^2. \quad (37)$$

For larger mass splittings, $\Delta m \gg 2m_\mu$, the decays proceed much more rapidly, as follows:

$$\Gamma_{\phi_2 \to \phi_1 \mu\mu} \approx 400\ \mathrm{s}^{-1} \left(\frac{g}{0.2}\right)^2 \left(\frac{\Delta m}{1\ \mathrm{GeV}}\right)^5 \left(\frac{\mathrm{TeV}}{m_{\phi_2}}\right)^2. \quad (38)$$

The total decay width further increases if we consider larger values of Δm, allowing other decay channels to become kinematically accessible.

Some of the most stringent constraints on long-lived particles follow from the ionization history of our Universe and its impact on the cosmic microwave background. In particular, such constraints can exclude decays to electromagnetic final states in the following range [42,43]:

$$10^{13}\ \mathrm{s} \lesssim \tau_{\phi_2} \lesssim 10^{25}\ \mathrm{s} \left(\frac{\Delta m}{m_{\phi_2}}\right). \quad (39)$$

In the regime of $\Delta m < 2m_e$ and $m_\phi \gtrsim 100$ GeV, the ϕ_2 lifetime is long enough to avoid these constraints over nearly all of our parameter space. These constraints do, however, rule out a portion of the parameter space in which $2m_e \leq \Delta m \leq 2m_\mu$.

If ϕ_2 decays produce photons or electrons with enough energy to disassociate helium nuclei (corresponding to $\Delta m \gtrsim 56.6$ MeV), these reactions could potentially impact the primordial helium and deuterium abundances [44,45]. These considerations constrain the parameter space in this model with $\Delta m \gtrsim 60$ MeV, $\tau_{\phi_2} \gtrsim 10^3$ s, and $\Delta m/m_{\phi_2} \gtrsim 10^{-5}$, corresponding to the requirement,

$$\Delta m \gtrsim 5\ \mathrm{GeV} \left(\frac{0.3}{g}\right)^{2/5} \left(\frac{m_{\phi_2}}{\mathrm{TeV}}\right)^{2/5}. \quad (40)$$

These constraints become significantly weaker for $\tau_{\phi_2} \lesssim 10^3$ s. For $\Delta m \gtrsim$ GeV, these decays are expected to be safe from all cosmological bounds.

These constraints could be further relaxed if processes such as $\phi_2 f \to \phi_1 f$ are able to deplete the ϕ_2 abundance before these particles can decay. If the rate for $\phi_2 \to \phi_1$ conversion is large compared to the Hubble rate, chemical equilibrium will be maintained between the ϕ_1 and ϕ_2 populations [46–48]. For $T \lesssim \Delta m$, this would lead to the exponential suppression of the heavier population, $n_{\phi_2}/n_{\phi_1} \approx e^{-\Delta m/T}$. The cross section for the $\phi_2 f \to \phi_1 f$ process is given by [14]

$$\sigma_{\phi_2 f \to \phi_1 f} = \frac{g^2 m_f^2}{32\pi E_{\phi_2} E_f |\vec{p}_i| v\sqrt{s}} \left[\log\left(\frac{m_h^2 - t^-}{m_h^2 - t^+}\right) - \frac{4|\vec{p}_i||\vec{p}_f|(m_h^2 - 4m_f^2)}{(m_h^2 - t^-)(m_h^2 - t^+)}\right], \quad (41)$$

where v is the relative velocity in the center-of-momentum frame, $\vec{p}_{i,f}$ are the initial and final momenta in this frame, $E_{\phi_2,f}$ are the particle energies, and $t^\pm$ is the Mandelstam variable evaluated at $\cos\theta = \pm 1$, where θ is the scattering angle (for complete expressions, see Appendix B of Ref. [14]). To obtain the thermal average, we use Eq. (33) and evaluate the rate $\Gamma_{\phi_2 f \to \phi_1 f} = n_f \langle \sigma v \rangle_{\phi_2 f \to \phi_1 f}$, where $n_f \propto T^3$ is the number density of target fermions. Numerically, we find that for the range of mass splittings and couplings considered here, this rate can easily exceed the Hubble rate for $\Delta m \gtrsim T \gtrsim m_\mu$. Due to the small Yukawa coupling involved, the corresponding scattering rate with electrons is typically too small to maintain kinetic equilibrium.

VI. INDIRECT DETECTION

DM particles annihilating in the Galactic Halo (or in other regions, such as within nearby dwarf galaxies) can lead to potentially observable fluxes of γ rays [22–24] and cosmic-ray antimatter [25–27], allowing us to place constraints on the DM's annihilation cross section. Within the

viable parameter space of this model, the relic abundance can be set by different combinations of coannihilations ($\phi_1\phi_2 \to hh, ZZ, WW, f\bar{f}$), ϕ_2 annihilations ($\phi_2\phi_2 \to hh, f\bar{f}$), and t-channel ϕ_1 annihilations ($\phi_1\phi_1 \to hh$). Since only the last of these processes contributes to the $\phi_1\phi_1$ annihilation rate, indirect detection signals will be highly suppressed if $m_\phi < m_h$. At higher masses, $m_\phi > m_h$, the magnitude of the annihilation rate depends on the mass and couplings of the DM, as well as on the mass splitting, Δm. For $m_\phi > m_h$, the cross section relevant for indirect detection is given by

$$\langle \sigma v \rangle_{\phi_1\phi_1 \to hh} \approx \frac{g^4 v_h^4}{64\pi m_\phi^3 (m_\phi^2 - m_h^2)^{3/2}} \sim 10^{-26}\,\mathrm{cm}^3\,\mathrm{s}^{-1} \left(\frac{g}{0.1}\right)^4 \left(\frac{150\,\mathrm{GeV}}{m_\phi}\right)^6, \quad (42)$$

where we have taken $f_1 \approx 0$.

A bright and statistically significant excess of GeV-scale emission has been detected from the region surrounding the Galactic Center [22,49–60]. The spectrum, angular distribution, and overall intensity of this signal is consistent with that expected from DM in the form of an annihilating thermal relic. It was shown in Ref. [61] that DM annihilating to a pair of Higgs bosons with $\langle \sigma v \rangle_{\phi_1\phi_1 \to hh} \sim 10^{-26}$ cm^3/s would provide a good match to this signal for masses in the range of $m_{\phi_1} \sim 125$–150 GeV [21,61]. In the same region of parameter space, DM annihilation could also produce the small excess of ∼10–20 GeV antiprotons that has been observed in the cosmic-ray spectrum [25,27,61–63]. For these reasons, this model is well suited to generate a signal consistent with the observed features of the Galactic Center γ-ray excess, as well as the excess of cosmic-ray antiprotons.

VII. ELECTROWEAK PHASE TRANSITION

The interaction between the Standard Model Higgs doublet and the complex singlet scalar field in this model can modify the Higgs potential at finite temperatures in a way that could potentially lead to a strong first-order EWPT in the early Universe. Such a phase transition could play a central role in generating the observed baryon asymmetry through electroweak baryogenesis [28–31],[3] and could result in the production of a stochastic background of gravitational waves.

[3]For electroweak baryogenesis to be viable, the Higgs sector must also exhibit explicit or spontaneous CP violation. In this study, we have assumed that no CP violation arises within the Higgs sector. However, this model could be straightforwardly extended, to include a Z_2 symmetric, CP-violating dimension-six operator of the form, $y_t \bar{Q}\tilde{H}(1 + ic\frac{\phi\phi^\star}{\Lambda^2})t_R + h.c.$, where y_t is the top Yukawa coupling and Λ is the cutoff scale [64–68].

A first-order EWPT can occur when the finite-temperature effective potential of the Higgs field develops at least two distinct local minima, separated by a potential barrier at temperatures above the critical temperature, T_c. At $T = T_c$, the two minima become degenerate in energy while remaining separated by this barrier. At one of these minima, electroweak symmetry remains unbroken, while it is broken at the other. As the Universe cools below T_c, a global minimum in the broken-symmetry phase develops, characterized by nonzero field values and a lower potential energy. The system, initially trapped in the symmetric (false vacuum) phase, can then transition into the broken (true vacuum) phase via quantum or thermal tunneling [69–71].

The transition into the true vacuum proceeds through the nucleation of bubbles in the broken phase within the symmetric thermal plasma. Once formed, these bubbles grow and eventually coalesce, thereby converting the remaining volume of space into the broken phase. The bubble nucleation rate per unit volume at finite temperature, in the semiclassical approximation, satisfies the following [72–74]:

$$\Gamma_B \propto T^4 \exp\left(-\frac{S_3(T)}{T}\right), \quad (43)$$

where $S_3(T)$ is the three-dimensional Euclidean action, as evaluated at the bounce configuration. For the phase transition to successfully complete, the nucleation rate must be sufficiently large to produce at least one bubble per Hubble volume, per Hubble time, as realized when $S_3(T) \sim 140T$ [71,75,76]. The corresponding nucleation temperature, $T_n(\lesssim T_c)$, is the highest temperature at which this condition is satisfied as the Universe cools. In our analysis, we compute the bounce solution and corresponding action using the path deformation algorithm, as implemented in the publicly available package, CosmoTransitions (v2.0.6) [77].

To facilitate successful electroweak baryogenesis, the electroweak sector must undergo a strong first-order phase transition, corresponding to the following criterion:

$$\xi_n = \frac{v_h(T_n)}{T_n} > 1, \quad (44)$$

where $v_h(T_n)$ is the VEV along the Standard Model Higgs field direction evaluated at the nucleation temperature, T_n. This condition ensures that any baryon asymmetry that is generated will not be washed out after the phase transition has ended.

To analyze the thermal evolution of the effective potential, one begins with the tree-level scalar potential at zero temperature, $V_0(h, \phi_1, \phi_2)$. From Eqs. (4)–(16), this potential can be expressed as

$$V_0 = -\frac{1}{2}\mu_h^2 h^2 + \frac{1}{4}\lambda_h h^4 + \frac{1}{2}\left(m_0^2 + \frac{1}{2}\kappa h^2\right)(\phi_1^2 + \phi_2^2) + \frac{1}{2}\left(\rho_{0_R}^2 + \frac{\eta_R}{2}h^2\right)(\phi_1^2 - \phi_2^2) - \left(\rho_{0_I}^2 + \frac{\eta_I}{2}h^2\right)\phi_1\phi_2 + \frac{1}{4}(\lambda_1\phi_1^4 + \lambda_2\phi_2^4 + \lambda_{12}\phi_1^2\phi_2^2)\Big), \tag{45}$$

where we have used the shorthand notation,

$$\eta_R = \mathrm{Re}(\eta), \qquad \eta_I = \mathrm{Im}(\eta)$$
$$\rho_{0_R}^2 = \mathrm{Re}(\rho_0^2), \qquad \rho_{0_I}^2 = \mathrm{Im}(\rho_0^2). \tag{46}$$

Here, we include quartic self-interactions for the singlet fields ϕ_1 and ϕ_2, parametrized by λ_1, λ_2, and λ_{12}. In the special case $\lambda_1 = \lambda_2 = \lambda_{12}$, the scalar sector exhibits an enhanced approximate $U(1)$ symmetry. Allowing these couplings to differ explicitly breaks this symmetry and provides additional freedom in shaping the scalar potential. In particular, the mixed quartic coupling λ_{12} controls the interaction between the two singlet directions and plays an important role in determining the structure of the potential barrier and the resulting phase transition pattern. We note that, for generic values of λ_1, λ_2, and λ_{12}, the singlet sector exhibits a $Z_2 \times Z_2$ symmetry under independent sign flips of ϕ_1 and ϕ_2. The Z_2 symmetry relevant for dark matter stability corresponds to the diagonal subgroup under which both fields transform simultaneously. The approximate $U(1)$ symmetry is already broken by the mass and Higgs portal terms, and allowing the quartic couplings to differ introduces additional explicit breaking without affecting the consistency of the model.

In this study, we will work in the limit of $\sin 2\theta = 0$, which implies $\rho_{0_I}^2 = -v_h^2\eta_I/2$. At zero temperature, V_0 is minimized for

$$\langle h\rangle = v_h, \quad \langle\phi_1\rangle = 0, \quad \langle\phi_2\rangle = 0. \tag{47}$$

The following quantities can be treated as the free parameters of the scalar potential given in Eq. (45):

$$m_{\phi_1}, \Delta m, f_1, f_2, g, \lambda_1, \lambda_2, \lambda_{12}. \tag{48}$$

Using Eqs. (14)–(16), the other parameters of the potential can be expressed as

$$\eta_I = -g, \qquad \kappa = f_2, \qquad \eta_R = -\kappa,$$
$$m_0^2 = \frac{1}{2}(m_{\phi_1}^2 + m_{\phi_2}^2 - \kappa v_h^2),$$
$$\rho_{0_R}^2 = \frac{1}{2}(m_{\phi_1}^2 - m_{\phi_2}^2 + \kappa v_h^2), \tag{49}$$

where we have taken $f_1 \approx 0$. The zero-temperature, tree-level potential given in Eq. (45) receives quantum corrections from all of the Standard Model degrees of freedom that couple to the h, ϕ_1, or ϕ_2 fields. A discussion of these corrections, as well as the finite-temperature corrections, is provided in Appendix B.

Since the Standard Model predicts a crossover EWPT, we must rely on interactions between the Higgs and $\phi_{1,2}$ fields to obtain a strong first-order phase transition. The coupling, f_1, is tightly constrained by direct detection experiments and must be quite small (see Fig. 1). In contrast, f_2 and g are not directly involved in DM-nucleon scattering at tree level and can be much larger. The impact of g on the Higgs thermal corrections is generally mild compared to that of f_2, as seen in Eq. (B18) of Appendix B. For these reasons, it is f_2 that generally plays the most important role in facilitating a strong first-order phase transition.

The thermal evolution of the scalar potential in this model can proceed through a different series of events, depending on the parameter values that are selected. In addition to the standard, one-step first-order phase transition, it is possible that this phase transition may have taken place in two distinct steps. In such a scenario, the fields ϕ_1 and ϕ_2 first acquire nonzero VEVs through a second- or first-order phase transition. This is followed by a first-order phase transition in which the Higgs field acquires a nonzero VEV while ϕ_1 and ϕ_2 eventually return to the symmetric phase with vanishing VEVs.

The residual Z_2 symmetry under which $\phi_i \to -\phi_i$ ensures the stability of the DM and forbids nonzero VEVs for either field at zero temperature. At high temperatures, however, these fields can temporarily develop nonzero VEVs due to thermal effects. The pattern of symmetry breaking in the singlet sector can be understood by examining the coefficients of their quadratic terms in the scalar potential, which can be derived from the field-dependent mass relations given in Eq. (B16). At finite temperature, prior to electroweak symmetry breaking, and in the limit $\lambda_{12} \approx 0$ and $\rho_{0_I}^2 \approx 0$, the following relations hold:

$$g \approx 0, \qquad m_{\phi_{1,2}}^2 \approx m_0^2 \pm \rho_{0_R}^2. \tag{50}$$

So, for $\rho_{0_R}^2 > m_0^2 > 0$, ϕ_2 can acquire a nonzero VEV, while ϕ_1 remains at the origin. Thus, depending on the sign and magnitude of $\rho_{0_R}^2$, only one of the singlet fields acquires a nonzero VEV. When $\rho_{0_I}^2$ (or equivalently, g) is nonzero, the $\rho_{0_I}^2\phi_1\phi_2$ term of the potential can result in a tadpole contribution which can lead to a nonzero VEV for the other field at finite temperature. At sufficiently high temperatures, however, large positive thermal mass corrections [see Eq. (B18) of Appendix B] can cause the coefficients of the quartic field terms to become positive, restoring the Z_2 symmetry.

The parameter, $\rho_{0_R}^2$, depends on the mass splitting, Δm, for a fixed value of f_2, making Δm a key driver of symmetry breaking in the singlet sector. For some values of Δm, the singlet fields never acquire nonzero VEVs at high temperatures, resulting in a one-step phase transition along the Higgs field direction. Conversely, in order for a two-step phase transition to occur, Δm and g must be appropriately tuned to allow ϕ_1 and ϕ_2 to develop nonzero VEVs. The nature of this phase transition along the singlet direction, whether second order or first order, depends on the strength of thermally induced cubic terms.

VIII. BENCHMARK SCENARIOS

In Table I, we present parameter values for two representative benchmark models, BP1 and BP2. For BP1, m_{ϕ_1} lies below m_h but above $m_h/2$, while for BP2, $m_{\phi_1} > m_h$. These specific choices for m_{ϕ_1} have distinct implications for DM detection.

For both benchmarks, the predicted spin-independent direct detection cross sections lie well below current bounds from LUX-ZEPLIN, while remaining within the projected sensitivity of next-generation experiments.

The indirect detection prospects, however, differ markedly between the two cases. For BP1, the condition $m_{\phi_1} < m_h$ kinematically forbids annihilation into Higgs boson pairs, resulting in $\langle\sigma v\rangle_{\phi_1\phi_1} \simeq 4.9 \times 10^{-30}$ cm^3/s, which is far below the sensitivity of current γ-ray and cosmic-ray searches. In contrast, for BP2 with $m_{\phi_1} = 130$ GeV, the $\phi_1\phi_1 \to hh$ channel is open and dominates the annihilation rate, yielding $\langle\sigma v\rangle_{\phi_1\phi_1} \simeq 1.6 \times 10^{-26}$ cm^3/s. This value lies in the range required to explain the Galactic Center γ-ray excess. A closely related scenario with $m_{\phi_1} \simeq 130$ GeV and dominant $\phi_1\phi_1 \to hh$ annihilation has been studied in detail in Ref. [21], where it was shown to provide an excellent fit to the Galactic Center excess spectrum, with a reported p value of ~0.6–0.7. Independently, it has been shown that annihilation cross sections of this size into hadronic final states are compatible with the alpha magnetic spectrometer (AMS-02) antiproton data [25,27,61]. Given the close correspondence between that setup and our BP2, we do not repeat the full likelihood analysis here, but instead rely on these established results for this mass range and annihilation channel.

Both benchmarks exhibit a two-step phase transition, whose numerical characteristics are given in Table II. In the first step, the singlet fields acquire nonzero VEVs, spontaneously breaking the Z_2-symmetry. Subsequently, at a lower temperature, a second phase transition breaks electroweak symmetry. This latter transition satisfies $\xi_n > 1$, which is a key requirement of electroweak baryogenesis. At the end of the second step, the singlet fields transition back to a state with zero VEVs, thereby restoring the Z_2-symmetry which ensures the stability of the DM.

TABLE II. Characteristics of the phase transitions predicted in our benchmark models, BP1 and BP2, as defined in Table I. Both of these models predict a second-order phase transition (S), which is followed by a first-order transition (F), the latter of which triggers electroweak symmetry breaking. Listed in this table are the values of the critical temperature, T_c, the nucleation temperature, T_n, and the field values at the false and true vacua. The values of ξ_n, α, and β/H_n are also provided in each case.

	T_i (GeV)		$\{h, \phi_1, \phi_2\}$		$\{h, \phi_1, \phi_2\}$			
	T_c	T_n	(False) (GeV)	$\xrightarrow[\text{type}]{\text{PT}}$	(True) (GeV)	ξ_n	α	β/H_n
BP1	343	343	$\{0, 0, 0\}$	S	$0, 1, 9$			
	90	69	$\{0, 29, 170\}$	F	$\{238, 0, 0\}$	3.4	0.13	420
BP2	257	257	$\{0, 0, 0\}$	S	$\{0, 1, 5\}$			
	121	109	$\{0, 21, 105\}$	F	$\{203, 0, 0\}$	1.9	0.035	2507

In Fig. 3, we plot the field values at various minima for the case of BP1. Each color in this figure represents a distinct minimum of the potential, and the lines depict phase evolution along different field directions as a function of temperature. The two-step transition involves three distinct phases, as indicated in Table II:

(i) Phase 1 (cyan line): the symmetric phase, in which all of the VEVs are equal to zero.
(ii) Phase 2 (red line): the Z_2 symmetry is broken ($\phi_1, \phi_2 \neq 0$), but electroweak symmetry remains unbroken ($h = 0$).
(iii) Phase 3 (magenta line): the phase in which electroweak symmetry is broken ($h \neq 0$), but the Z_2 symmetry is restored ($\phi_1 = \phi_2 = 0$).

At high temperatures, the system starts in the symmetric phase with all scalar fields at the origin. As the Universe cools, a second-order transition occurs at $T = 343$ GeV and the singlet fields develop nonzero VEVs as the system moves to Phase 2. In the left frame, the black point between Phase 1 and Phase 2 indicates that the field, h, remains unchanged during this transition, while the black arrow in the right plot shows that ϕ_1 and ϕ_2 develop nonzero VEVs. At a lower temperature, the electroweak symmetry-breaking minimum (Phase 3) develops. The blue arrow marks the transition path at the nucleation temperature, $T_n = 69$ GeV, where the system tunnels from Phase 2 to Phase 3. The value of h reaches 246 GeV at $T = 0$.

This sequence of events has important cosmological implications. In the parameter space featuring a two-step phase transition, the Z_2 symmetry is spontaneously broken by thermal effects when ϕ_1 and ϕ_2 acquire nonzero VEVs, leading to the formation of potentially problematic domain walls. If these domain walls were to persist to later times, they would come to dominate the energy density of the Universe and spoil the success of the standard cosmological model. During the second step of our phase transition, however, ϕ_1 and ϕ_2 return to the origin of field space, resulting in the destruction of these domain walls at early times [64,78].

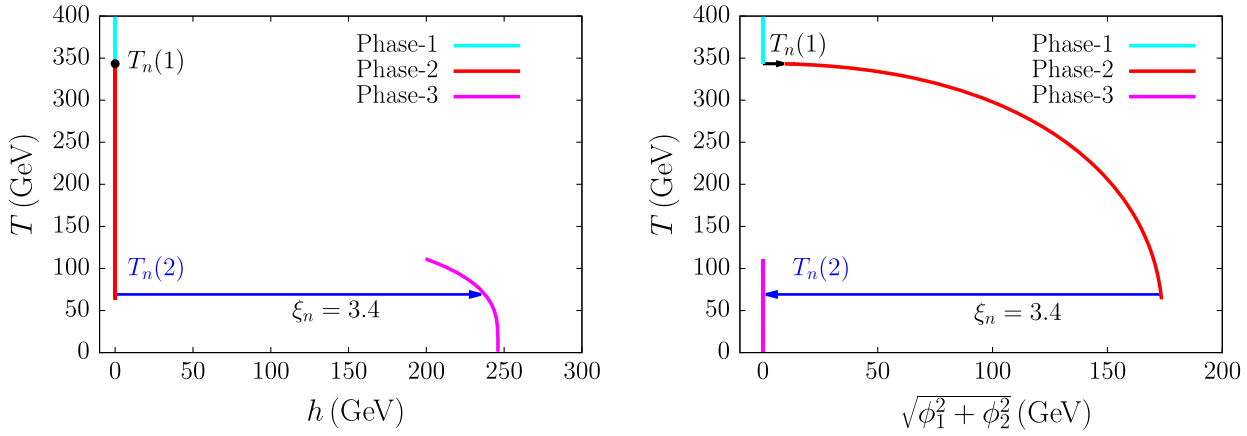


FIG. 3. Evolution of the field values in the case of our benchmark model, BP1. Each color represents a distinct minimum of the potential, and the lines describe the phase evolution along different field directions as a function of temperature. The left and right plots illustrate BP1's phase evolution along the Standard Model Higgs field, h, and the singlet direction, $\sqrt{\phi_1^2 + \phi_2^2}$, respectively. Arrows indicate the transition path from the false vacuum to the true vacuum, as calculated at the nucleation temperature, T_n. The black point in the left plot highlights the transition during which the corresponding field values exhibit minimal variation.

In some region of parameter space, the nucleation of electroweak bubbles within domain walls could accelerate the phase transition process [79,80], potentially modifying the nucleation temperature, T_n, and the resulting gravitational wave spectrum. A detailed study of these effects is beyond the scope of this work and is left for future investigation. Here, we assume that the bubbles grow homogeneously and neglect the impact of any domain walls on the resulting phase transition.

IX. GRAVITATIONAL WAVES

A first-order phase transition could result in the generation of a potentially observable stochastic background of gravitational waves. Such a signal would represent a way to probe the dynamics of the phase transitions that took place in the early Universe. The theoretical framework for estimating the amplitude of gravitational waves from a first-order phase transition is described in Appendix C.

The key parameters that govern the properties of this signal are

$$\alpha, \quad T_n, \quad \beta/H_n, \quad v_w, \tag{51}$$

where $\alpha = \Delta\rho/\rho_{\rm rad}$ is the ratio of the latent heat released to the radiation density, T_n is the nucleation temperature, β/H_n is the ratio of the bubble nucleation rate to the Hubble rate evaluated at T_n, and v_w is the wall velocity. The parameter values used in our benchmark models are summarized in Table II. Here, we consider $v_w \sim 1$, assuming that the expanding bubbles attain a relativistic terminal velocity in the plasma.

As detailed in Appendix C, the spectrum of the resulting gravitational waves receives contributions from three primary sources: (1) collisions of expanding bubbles, (2) sound waves from bubbles expanding through the plasma, and (3) magnetohydrodynamic (MHD) turbulence. The peak frequency and overall amplitude of the resulting gravitational wave spectrum are primarily determined by the energy density and wavelength of the sound waves.

The gravitational wave spectra that result in our benchmark models, BP1 and BP2, as calculated using Eqs. (C5)–(C12), are shown in Fig. 4. These predictions are compared to the projected sensitivities of several proposed space-based detectors, including LISA (laser interferometer space antenna) [81], ALIA (advanced laser interferometer antenna) [82], Taiji [83], BBO (big bang observer) [84], and U-DECIGO (ultimate deci-hertz interferometer gravitational wave observatory) [85].

To quantify detectability, we evaluate the SNR, defined as [86–88]

$$\mathrm{SNR} = \sqrt{\delta\mathcal{T}\int_{f_{\rm min}}^{f_{\rm max}} df \left[\frac{h^2\Omega_{\rm GW}(f)}{h^2\Omega_{\rm exp}(f)}\right]^2}, \tag{52}$$

where δ denotes the number of independent channels (e.g., $\delta = 1$ for LISA and $\delta = 2$ for BBO and U-DECIGO), and $\mathcal{T}$ is the mission duration, taken here to be $\mathcal{T} = 5$ years. The quantity $h^2\Omega_{\rm exp}(f)$ represents the effective noise power spectral density of the experiment. A gravitational wave (GW) signal is considered detectable if the SNR exceeds a threshold value that depends on the detector configuration. For LISA, this threshold is typically SNR ~ 50 for a four-link design and ~ 10 for a six-link configuration [86].

While we compute the SNR explicitly for LISA, which serves as the standard benchmark for space-based gravitational wave detectors with well-defined sensitivity and detection criteria, the situation is less clear for future experiments such as BBO and U-DECIGO. For these detectors, the precise SNR thresholds depend on the specific mission configuration and data analysis strategy, and are not yet universally established. For this reason, we

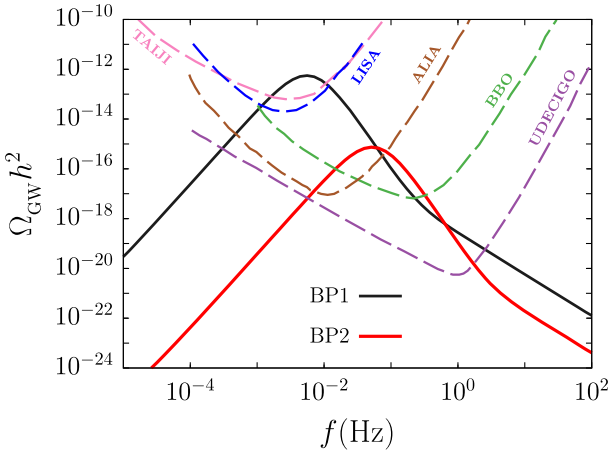


FIG. 4. Gravitational wave energy density spectra predicted for our benchmark models, BP1 and BP2. These results are compared to the projected sensitivities of the proposed gravitational wave detectors LISA, Taiji, ALIA, BBO, and U-DECIGO.

primarily use LISA to quantify detectability through the SNR, while for other proposed experiments we rely on a qualitative comparison between the predicted gravitational wave spectra and their projected sensitivity curves.

With this in mind, we find SNR = 29.2 for BP1 and SNR = 0.005 for BP2 in the case of LISA. Taking a representative detection threshold of SNR = 10, BP1 is potentially observable, whereas BP2 is not detectable by LISA, as can be seen from Fig. 4, where the gravitational wave spectrum of BP2 lies well below the LISA sensitivity curve over the entire frequency range, and therefore does not enter the detectable region. Nevertheless, BP2 may still lie within the sensitivity reach of more advanced future detectors such as BBO and U-DECIGO, as indicated by the comparison with their projected sensitivity curves.

X. COLLIDER PRODUCTION

Probing the physics of the Higgs sector is a key priority for existing and future high-energy colliders, including the LHC [89], Future Circular Collider, electron-positron [90], FCC-hh (hadron-hadron) [91], ILC (international linear collider) [92], and a muon collider [93]. An important part of this program is measurement of the invisible width of the Higgs, as well as other exotic decay channels [94].

For $m_{\phi_1}, m_{\phi_2} \lesssim m_h/2$, the dominant new Higgs decay channels in this model are $h \to \phi_1\phi_2$ and $h \to \phi_2\phi_2$, which arise from the couplings g and f_2, respectively ($h \to \phi_1\phi_1$ is suppressed by the small value of f_1 required to satisfy direct detection constraints). Note that the value of g also governs the DM's thermal relic abundance in the coannihilation limit, allowing us to place a lower limit on the branching fraction to $\phi_1\phi_2$ from relic abundance considerations. The upper bound on the Higgs invisible branching fraction from the LHC ($\lesssim$0.11) [95–97] constrains a substantial portion of the $m_\phi < m_h/2$ parameter space in this model [13,14,19].

For heavier DM, ϕ_1 and ϕ_2 can be produced through off-shell, Higgs-mediated processes, as follows:

$$pp \to h^\star X \to \phi_1\phi_2 X,$$
$$pp \to h^\star X \to \phi_2\phi_2 X, \tag{53}$$

where X represents an associated Standard Model object, such as a hard initial-state jet or photon. Again, the production of $\phi_1\phi_1$ is suppressed by the small value of f_1.

Although decays of the form $\phi_2 \to \phi_1 + \text{SM}$ could lead to distinctive signatures, the lifetime for this process is too long in much of the parameter space under consideration to be observed at colliders. If the mass splitting is sufficiently large, however, the ϕ_2 lifetime could be short enough to be observed at the LHC [98], or at future experiments such as massive timing hodoscope for ultra-stable neutral particles [99], as discussed in Ref. [14]. Even larger mass splittings could be probed at the LHC by focusing on final states with a hard jet/photon, large transverse missing energy, and additional Standard Model particles from ϕ_2 decays [100].

XI. CONCLUSIONS

Minimal scalar dark matter with a Higgs portal coupling offers a compelling and highly predictive scenario for thermal freeze-out. This model, however, has been almost entirely excluded by direct detection experiments. In this paper, we have presented a simple and viable variation of this scenario in which a *complex* scalar field couples to the Higgs portal through operators that explicitly break this field's global $U(1)$ symmetry. In the mass basis, the complex field decomposes into two nondegenerate eigenstates, ϕ_1 and ϕ_2. The heavier of these two states is unstable, while the lighter state can serve as a dark matter candidate. In selected regions of parameter space, the leading Higgs portal interaction can be off diagonal, leading to inelastic scattering with nuclei, and greatly relieving the tension with direct detection experiments.

The thermal relic abundance of dark matter in this model is governed by both annihilation and coannihilation processes. We have identified regions of parameter space in this model with $\phi_1 \sim 125$–150 GeV that predict a signal which is consistent with the observed features of the Galactic Center γ-ray excess.

The interactions of ϕ_1 and ϕ_2 in this model modify the shape of the Higgs potential, potentially facilitating a strong first-order electroweak phase transition. In addition to being necessary for successful electroweak baryogenesis, such a transition could lead to a potentially observable background of gravitational waves. In the minimal Higgs portal model, a strong first-order electroweak phase transition would require a value of the portal coupling that is ruled out by direct detection constraints. In contrast, large portal couplings are phenomenologically viable in this model, making it possible to modify the Higgs potential in

a way that could allow for a strong first-order phase transition.

ACKNOWLEDGMENTS

We thank Paddy Fox and Carlos Wagner for helpful conversations. D. H. is supported by the Office of the Vice Chancellor for Research at the University of Wisconsin-Madison, with funding from the Wisconsin Alumni Research Foundation. Fermilab is operated by the Fermi Research Alliance, LLC under Contract No. DE-AC02-07CH11359 with the U.S. Department of Energy, Office of Science, Office of High Energy Physics. D. R. is supported by the U.S. Department of Energy, Office of Science, Office of Workforce Development for Teachers and Scientists, Office of Science Graduate Student Research (SCGSR) program. The SCGSR program is administered by the Oak Ridge Institute for Science and Education for the DOE under Contract No. DE-SC0014664. S. R. is supported by the U.S. Department of Energy under Contract No. DEAC02-06CH11357 at the Argonne National Laboratory. S. R. would like to thank the University of Chicago, Fermilab, the Aspen Center for Physics, and the Perimeter Institute for Theoretical Physics, where a significant part of this work was carried out.

DATA AVAILABILITY

There are no publicly available research data or software supporting this manuscript. Requests for further information or data should be sent to the authors.

APPENDIX A: DIRECT DETECTION AT ONE LOOP

The tree-level direct detection cross section for elastic, spin-independent, $\phi_1 N \to \phi_1 N$ scattering is governed by f_1, which is chosen to be small in our benchmark scenarios. There are loop corrections to this process, however, which depend instead on g and/or f_2.

The main loop diagrams that contribute to this process include a triangle correction to the $\phi_1\phi_1 h$ vertex. For the process $\phi_1(p)N(k) \to \phi_1(p')N(k')$, the one-loop vertex contribution, δf_1, is given by

$$2\delta f_1 v = (-igv)^2(I_1 + I_2), \tag{A1}$$

where the integrals corresponding to the two scalar triangles are

$$I_1 \approx -\frac{3im_h^2}{v}\int \frac{d^4\ell}{(2\pi)^4}\frac{1}{(\ell^2 - m_h^2)^2[(\ell+p)^2 - m_{\phi_2}^2]}, \tag{A2}$$

$$I_2 \approx -2if_2 v\int \frac{d^4\ell}{(2\pi)^4}\frac{1}{(\ell^2 - m_{\phi_2}^2)^2[(\ell+p)^2 - m_h^2]}, \tag{A3}$$

where $q = p - p'$ is the nonrelativistic momentum transfer, and we have dropped terms of order q^2/m_h^2 and $q^2/m_{\phi_2}^2$. Using dimensional regularization, the vertex correction is

$$2\delta f_1 v = -\frac{i(gv)^2}{32\pi^2}\left(\frac{3m_h^2}{v}\Delta_1 + 2f_2 v\Delta_2\right), \tag{A4}$$

where we have defined the Feynman parameter integrals,

$$\Delta_1 = \int_0^1 dx \frac{2(1-x)}{x^2 m_{\phi_1}^2 + (1-x)m_{\phi_2}^2 - x(m_{\phi_1}^2 - m_h^2)}, \tag{A5}$$

$$\Delta_2 = \int_0^1 dx \frac{2(1-x)}{x^2 m_{\phi_1}^2 + (1-x)m_h^2 - x(m_{\phi_1}^2 - m_{\phi_2}^2)}, \tag{A6}$$

and the full amplitude for this process is

$$i\mathcal{M} \approx \frac{2v(f_1 + \delta f_1)y_N}{m_h^2}[\bar{u}(k')u(k)], \tag{A7}$$

where $y_N \sim m_N/v$ is the effective Higgs-nucleon coupling and u is a four-component spinor. Since we require $f_1 \ll 1$, the loop contribution to this process can be written as

$$\sigma_{\phi_1 N}^{\mathrm{SI,loop}} \approx \frac{|\delta f_1|^2 y_N^2 m_N^2}{\pi m_h^4 m_{\phi_2}^2}. \tag{A8}$$

We have numerically verified that the parameter choices for our benchmarks in Table I are safe from direct detection bounds, predicting values of order $\sigma_{\phi_1 N}^{\mathrm{SI,loop}} \sim 10^{-49}$ cm^2.

For completeness, we note that there is also a box diagram that enables $\phi_1 N \to \phi_1 N$ scattering through double-Higgs exchange. We have numerically verified that this contribution is subdominant to the (already small) contributions from the vertex loop, and we do not consider it further in our analysis.

APPENDIX B: HIGGS POTENTIAL AT FINITE TEMPERATURE

The one-loop radiative corrections to the zero-temperature tree-level potential, defined in Eq. (45), can be expressed in terms of the well-known Coleman-Weinberg (CW) [101] potential. In the $T = 0$ limit, this takes the following form:

$$V_{\mathrm{CW}}(m_i^2) = \sum_i (-1)^{2s_i}\frac{n_i m_i^4}{64\pi^2}\left(\ln\frac{m_i^2}{Q^2} - C_i\right), \tag{B1}$$

where $m_i \equiv m_i(h, \phi_1, \phi_2)$, Q is the renormalization scale (which we take to be the electroweak scale, $Q = v_h$), and the sum is performed over all the particles in the model. The constants, C_i, depend on the choice of the renormalization scheme. In this work, we adopt the $\overline{\mathrm{MS}}$ on-shell scheme, for

which $C_{W^\pm,Z} = 5/6$ and $C_i = 3/2$ for all other particle species. Here, m_i is the tree-level field-dependent mass of the ith species, and n_i and s_i are their associated numbers of degrees of freedom and spin, respectively.

The one-loop CW correction to the tree-level potential alters the masses and mixing angles of the scalar degrees of freedom and shifts the position of the electroweak minimum in field space. To keep them fixed at tree-level, we modify the $\overline{\text{MS}}$ CW potential by adding suitable counterterms, V_{CT}, to the potential, which satisfy

$$V_{\text{CT}} = -\frac{1}{2}\delta\mu_h^2 h^2 + \frac{1}{4}\delta\lambda_h h^4 + \delta m^2_{h\phi_1} h\phi_1 + \delta m^2_{h\phi_2} h\phi_2 + \delta m^2_{\phi_1\phi_2}\phi_1\phi_2 + \frac{1}{4}\delta\lambda_{h\phi_1} h^2\phi_1^2 + \frac{1}{4}\delta\lambda_{h\phi_2} h^2\phi_2^2. \quad \text{(B2)}$$

The various coefficients in this expression are fixed by imposing the following on-shell renormalization conditions at zero-temperature:

$$\frac{\partial(V_{\text{CW}} + V_{\text{CT}})}{\partial y_i} = 0, \qquad \frac{\partial^2(V_{\text{CW}} + V_{\text{CT}})}{\partial y_i \partial y_j} = 0, \quad \text{(B3)}$$

where $\{y_1, y_2, y_3\} = \{\phi_1, \phi_2, h\}$. All first and second derivatives are evaluated at the true electroweak minimum field values, $\{\phi_1, \phi_2, h\} = \{0, 0, v_h\}$. The coefficients of the counterterms are related to the derivatives of the potential as follows:

$$\delta\mu_h^2 = \frac{3V_h}{2v} - \frac{V_{hh}}{2}, \qquad \delta\lambda_h = \frac{V_h}{2v^3} - \frac{V_{hh}}{2v_h^2}, \quad \text{(B4)}$$

$$\delta m^2_{h\phi_1} = -\frac{V_{\phi_1}}{v}, \qquad \delta m^2_{\phi_1\phi_2} = -V_{\phi_1\phi_2}, \qquad \delta m^2_{h\phi_2} = -\frac{V_{\phi_2}}{v}, \quad \text{(B5)}$$

$$\delta\lambda_{h\phi_1} = -\frac{2V_{\phi_1\phi_1}}{v_h^2}, \qquad \delta\lambda_{h\phi_2} = -\frac{2V_{\phi_2\phi_2}}{v_h^2}, \quad \text{(B6)}$$

where we have defined

$$V_{y_i} \equiv \frac{\partial V_{\text{CW}}}{\partial y_i}, \qquad V_{y_i y_j} \equiv \frac{\partial^2 V_{\text{CW}}}{\partial y_i \partial y_j}. \quad \text{(B7)}$$

Note that the Goldstone modes have vanishing masses at the true, zero-temperature electroweak minimum. This leads to an infrared divergence [102,103] stemming from the second derivative used in the renormalization conditions found in Eq. (B3). To address this, an infrared regulator can be introduced by modifying the Goldstone mode masses as $m_G^2 \to m_G^2 + \mu_{\text{IR}}^2$. In this study, we follow the approach outlined in Refs. [68,104–108] and set $\mu_{\text{IR}}^2 = 1\ \text{GeV}^2$.

At finite temperatures, the effective potential receives additional corrections which, at the one-loop level, are given by [109–111]

$$V_{\text{TH}}(m_i^2, T) = \frac{T^4}{2\pi^2}\sum_i n_i J_{B,F}\left[\frac{m_i^2(h,\phi_1,\phi_2)}{T^2}\right]. \quad \text{(B8)}$$

The thermal functions, $J_{B(F)}$, are defined as

$$J_{B(F)}(y^2) = \pm\text{Re}\int_0^\infty x^2 \ln\left(1 \mp \exp^{-\sqrt{x^2+y^2}}\right)dx, \quad \text{(B9)}$$

where the lower (upper) sign corresponds to fermions (bosons), and the sum is performed over all particles, as described in Eq. (B1).

In the high-temperature limit, $m_i^2 \ll T^2$, the thermal functions can be expanded to $\mathcal{O}(y^6)$ as

$$J_B(y^2) \approx -\frac{\pi^4}{45} + \frac{\pi^2}{12}y^2 - \frac{\pi}{6}y^3 - \frac{1}{32}y^4\log\left(\frac{y^2}{a_B}\right), \quad \text{(B10)}$$

$$J_F(y^2) \approx \frac{7\pi^4}{360} - \frac{\pi^2}{24}y^2 - \frac{1}{32}y^4\log\left(\frac{y^2}{a_F}\right), \quad \text{(B11)}$$

where we have defined

$$a_B = 16\pi^2\exp\left(\frac{3}{2} - 2\gamma_E\right), \qquad a_F = \frac{a_B}{16}, \quad \text{(B12)}$$

and $\gamma_E \approx 0.577$ is the Euler-Mascheroni constant. The presence of the $-\pi y^3/6$ term in the high-temperature expansion of J_B can result in an energy barrier between two degenerate vacua, thus allowing for a strong first-order phase transition. Note that such a cubic term appears only for bosonic degrees of freedom, as it arises from the (Matsubara) zero mode propagator. This term is associated with divergences in the infrared limit. Thus, at high temperatures, the perturbative expansion of the effective potential breaks down. This issue can be resolved by resumming a set of higher-loop diagrams, commonly known as daisy contributions.

Various resummation techniques have been developed to address this infrared problem by incorporating higher-order thermal corrections [112–115] (for a more detailed discussion, see Ref. [108]). Among these, we adopt the Parwani prescription [113] in this work. We denote the temperature- and field-dependent masses as M_i^2, where

$$M_i^2 = \text{Eigenvalues}[M_{kl}^2], \qquad M_{kl}^2 \equiv m_{kl}^2 + \Pi(T^2), \quad \text{(B13)}$$

and $\Pi(T^2) = c_{kl}T^2$, where c_{kl}s are the so-called daisy coefficients. In this scheme, m_i^2 is replaced by the temperature-dependent mass, M_i^2, in the one-loop CW correction and in the one-loop thermal correction potential.

The temperature-dependent effective potential at one-loop order is thus given by

$$V_{\rm eff} = V_0 + V_{\rm CW}(M_i^2) + V_{\rm CT} + V_{\rm TH}(M_i^2, T). \quad \text{(B14)}$$

The EWPT can be studied by monitoring the evolution of the minimum of this potential as a function of temperature. The production of gravitational waves from a first-order phase transition will be discussed in Appendix C.

The field-dependent tree-level mass-squared matrix for the CP-even scalar sector can be obtained from the scalar potential:

$$m^2_{y_i y_j} \equiv \frac{\partial^2 V_0}{\partial y_i \partial y_j}, \quad \text{(B15)}$$

where $\{y_1, y_2, y_3\} = \{\phi_1, \phi_2, h\}$. Its components in this basis are given explicitly by

$$\begin{aligned}
m^2_{hh} &= -\mu_h^2 + 3\lambda_h h^2 + \frac{\eta_I}{2}\phi_1\phi_2 + \frac{\kappa}{2}(\phi_1^2+\phi_2^2) + \frac{\eta_R}{2}(\phi_1^2-\phi_2^2),\\
m^2_{\phi_1\phi_1} &= m_0^2 + \frac{\kappa+\eta_R}{2}h^2 + \rho^2_{0_R} + \frac{\lambda_{12}}{2}\phi_2^2 + 3\lambda_1\phi_1^2,\\
m^2_{\phi_2\phi_2} &= m_0^2 + \frac{\kappa-\eta_R}{2}h^2 - \rho^2_{0_R} + \frac{\lambda_{12}}{2}\phi_1^2 + 3\lambda_2\phi_2^2,\\
m^2_{h\phi_1} &= m^2_{\phi_1 h} = \kappa h\phi_1 + \eta_R h\phi_2 - \eta_I h\phi_2,\\
m^2_{h\phi_2} &= m^2_{\phi_2 h} = \kappa h\phi_2 - \eta_R h\phi_1 - \eta_I h\phi_1,\\
m^2_{\phi_1\phi_2} &= m^2_{\phi_2\phi_1} = -\rho^2_{0_I} - \frac{1}{2}\eta_I h^2 + \lambda_{12}\phi_1\phi_2. \quad \text{(B16)}
\end{aligned}$$

The field-dependent squared masses of the Goldstone modes, gauge bosons, and top quark are given by

$$\begin{aligned}
m^2_{G^0,G^\pm} &= -\mu_h^2 + \lambda_h h^2, \qquad m^2_{W^\pm} = \frac{1}{4}g_2^2 h^2,\\
m^2_Z &= \frac{1}{4}(g_1^2+g_2^2)h^2, \qquad m_t^2 = \frac{1}{2}y_t^2 h^2.
\end{aligned}$$

The daisy coefficients can be derived using Eq. (B10) from the high-temperature expansion of the thermal one-loop potential, as follows:

$$c_{kl} = \frac{1}{T^2}\frac{\partial^2 V_{\rm TH}}{\partial y_k \partial y_l}\bigg|_{T^2 \gg m^2}, \quad \text{(B17)}$$

where we have obtained

$$\begin{aligned}
c_{hh} &= \frac{1}{16}(3g_2^2+g_1^2) + \frac{1}{4}y_t^2 + \frac{1}{48}(24\lambda_h + 4\kappa - \eta_I),\\
c_{\phi_1\phi_1} &= \frac{1}{24}(8\kappa + 4\eta_R + 6\lambda_1 + \lambda_{12}),\\
c_{\phi_2\phi_2} &= \frac{1}{24}(8\kappa - 4\eta_R + 6\lambda_2 + \lambda_{12}). \quad \text{(B18)}
\end{aligned}$$

To obtain the eigenvalues of the temperature-dependent mass-squared matrix, these corrections, $c_{kl}T^2$, are added to the expressions for m^2_{kl}, as given in Eq. (B16). Similarly, thermal correction, $c_{hh}T^2$, must be added to the mass-squared terms for the Goldstone modes.

The temperature-dependent squared mass of $W_L^\pm$ is given by

$$M^2_{W_L^\pm} = \frac{1}{4}g_2^2 h^2 + \frac{11}{6}g_2^2 T^2. \quad \text{(B19)}$$

Lastly, the thermal corrections for the longitudinal component of the Z boson and photon fields can be obtained by diagonalizing the following matrix:

$$\frac{1}{4}h^2\begin{pmatrix} g_2^2 & -g_2 g_1 \\ -g_1 g_2 & g_1^2 \end{pmatrix} + \begin{pmatrix} \frac{11}{6}g_2^2 T^2 & 0 \\ 0 & \frac{11}{6}g_1^2 T^2 \end{pmatrix}. \quad \text{(B20)}$$

APPENDIX C: GRAVITATIONAL WAVE PRODUCTION FROM A FIRST-ORDER PHASE TRANSITION

A first-order phase transition in the early Universe could potentially result in an observable stochastic background of gravitational waves. Unlike gravitational waves originating from binary systems, the stochastic background is unpolarized and isotropic, with an amplitude that follows a Gaussian distribution [116]. Consequently, it can be characterized by a two-point correlation function that is proportional to the power spectral density, $\Omega_{\rm GW}h^2$. The detection of a stochastic gravitational wave background would generally require the identification of a cross correlation across multiple detectors [86,117–120].

The dimensionless parameter, α, can be written as [121]

$$\alpha \equiv \frac{\Delta\rho}{\rho_{\rm rad}} = \frac{1}{\rho_{\rm rad}}\left(\frac{T}{4}\frac{d\Delta V}{dT} - \Delta V\right), \quad \text{(C1)}$$

where ΔV is the difference between the potential energies at the false and true minima, and all quantities in this expression are evaluated at the completion of the phase transition. In the absence of appreciable entropy injection during the phase transition, we typically expect the phase transition to end at a temperature that is approximately equal to the nucleation temperature. The nucleation temperature can be found by solving the following equation:

$$\int_{T_n}^{\infty}\frac{dT}{T}\frac{\Gamma(T)}{H(T)^4} \approx 1, \quad \text{(C2)}$$

where $\Gamma(T)$ is the tunneling probability from the false vacuum to the true vacuum per unit time and volume [122]. To compute this quantity, it is necessary to solve for the bounce solution of the so-called Euclidean action, $S_3(T)$ [71]. For this purpose, we have employed the publicly available package, CosmoTransitions [77].

Equation (C2) identifies the temperature at which the nucleation probability of a single bubble within a horizon

volume becomes approximately equal to unity. This approximately translates to the criterion, $S_3(T)/T \approx 140$. Solving this equation allows one to determine T_n, which corresponds to the maximum temperature at which $S_3/T \lesssim 140$ [123].

The inverse of the duration of the phase transition, β, is given by

$$\beta = -\frac{dS_3}{dt} \simeq \frac{1}{\Gamma}\frac{d\Gamma}{dt} = HT\frac{d(S_3/T)}{dT}, \tag{C3}$$

where the quantities in this expression are evaluated at the end of the phase transition.

The energy that is released during the phase transition is shared between the plasma's kinetic energy, which causes a bulk motion of the fluid in the plasma resulting in gravitational waves, and the heating of the plasma. The parameter, κ_v, quantifies the fraction of the energy in latent heat that is converted into the bulk motion of the fluid. This can be estimated by [121]

$$\kappa_v \approx \left[\frac{\alpha}{0.73 + 0.083\sqrt{\alpha} + \alpha}\right]. \tag{C4}$$

Finally, κ_t is the fraction of κ_v that goes into the generation of MHD turbulence in the plasma. It is expected that $\kappa_t \approx (0.05\text{–}0.1)\kappa_v$ [124], and we adopt a value of $\kappa_t/\kappa_v = 0.1$ in our calculations.

Stochastic gravitational waves arising from a cosmological first-order phase transition can be generated through three primary mechanisms: bubble wall collisions, long-lasting sound waves in the plasma, and MHD turbulence. In the case of bubble collisions, gravitational waves are produced by the stress-energy tensor associated with the bubble wall [125–128]. For a phase transition occurring in a thermal plasma, however, the contribution from bubble collisions is negligible compared to the total gravitational wave energy density [129]. In contrast, the bulk motion of the plasma gives rise to velocity perturbations which lead to the generation of sound waves in a relativistic particle medium. These sound waves carry away the majority of the energy that is released during the phase transition [86,124,130–133]. Additionally, the percolation of the plasma can induce MHD turbulence due to the ionized nature of the plasma, further contributing to the production of gravitational waves [134–139].

By combining the contributions from sound waves and MHD turbulence, one can estimate the total gravitational wave intensity, $\Omega_{\rm GW}h^2$. The contribution of sound waves to the overall gravitational wave power spectrum can be described using the following fitting formula [140]:

$$\Omega_{\rm sw}h^2 = 3\times 10^{-6}\Upsilon_{\rm sw}v_w\left(\frac{H}{\beta}\right)\left(\frac{\kappa_v\alpha}{1+\alpha}\right)^2 G(f), \tag{C5}$$

where H is the Hubble rate evaluated at the temperature at the end of gravitational waves production (which we take to be equal to T_n), and we define

$$G(f) \equiv (f/f_{\rm sw})^3\left[\frac{7}{4+3(f/f_{\rm sw})^2}\right]^{7/2}. \tag{C6}$$

The present day peak frequency of the sound wave contribution is given by

$$f_{\rm sw} = 2\times 10^{-5}\ {\rm Hz}\left(\frac{1}{v_w}\right)\left(\frac{\beta}{H}\right)\left(\frac{T_n}{100\ {\rm GeV}}\right). \tag{C7}$$

The finite lifetime of the sound waves leads to a reduction in $\Omega_{\rm sw}h^2$, represented by the suppression factor, $\Upsilon(\tau_{\rm sw})$, appearing in Eq. (C5) [141,142]. This suppression factor is given by

$$\Upsilon_{\rm sw} = 1 - \frac{1}{\sqrt{1+2\tau_{\rm sw}H}}. \tag{C8}$$

The lifetime, $\tau_{\rm sw}$, is evaluated at the timescale over which the turbulence develops, approximately given by $\tau_{\rm sw} \sim R/\bar{U}_f$, where R is the mean bubble separation and $\bar{U}_f$ is the rms of the fluid velocity [143,144]. R is related to the duration of the phase transition, $R = (8\pi)^{1/3}v_w/\beta$ [140,141]. On the other hand, from hydrodynamic analyses, Refs. [140,145] have shown that the rms fluid velocity can be expressed as $\bar{U}_f = \sqrt{3\kappa_v\alpha/4}$. In the limit of $\tau_{\rm sw} \to \infty$, $\Upsilon_{\rm sw}$ approaches an asymptotic value of unity.

The contribution from MHD turbulence to the production of gravitational waves can be expressed as [86]

$$\Omega_t h^2 = 3\times 10^{-4}\left(\frac{H}{\beta}\right)\left(\frac{\kappa_t\alpha}{1+\alpha}\right)^{3/2} Q(f), \tag{C9}$$

where we have defined

$$Q(f) = \frac{(f/f_t)^3}{(1+f/f_t)^{11/3}(1+8\pi f/f_\star)}, \tag{C10}$$

and where the present day peak frequency of the turbulence-induced gravitational wave spectrum, f_t, is defined as

$$f_t = 3\times 10^{-2}\ {\rm mHz}\left(\frac{1}{v_w}\right)\left(\frac{\beta}{H}\right)\left(\frac{T}{100\ {\rm GeV}}\right), \tag{C11}$$

and where

$$f_* = 1.7\times 10^{-5}\ {\rm Hz}\left(\frac{T_n}{100\ {\rm GeV}}\right). \tag{C12}$$

[1] V. Silveira and A. Zee, Scalar phantoms, Phys. Lett. **161B**, 136 (1985).
[2] J. McDonald, Gauge singlet scalars as cold dark matter, Phys. Rev. D **50**, 3637 (1994).
[3] C. P. Burgess, M. Pospelov, and T. ter Veldhuis, The minimal model of nonbaryonic dark matter: A singlet scalar, Nucl. Phys. **B619**, 709 (2001).
[4] D. O'Connell, M. J. Ramsey-Musolf, and M. B. Wise, Minimal extension of the standard model scalar sector, Phys. Rev. D **75**, 037701 (2007).
[5] J. M. Cline, K. Kainulainen, P. Scott, and C. Weniger, Update on scalar singlet dark matter, Phys. Rev. D **88**, 055025 (2013); **92**, 039906(E) (2015).
[6] M. Duerr, P. Fileviez Perez, and J. Smirnov, Scalar singlet dark matter and gamma lines, Phys. Lett. B **751**, 119 (2015).
[7] M. Duerr, P. Fileviez Pérez, and J. Smirnov, Scalar dark matter: Direct vs Indirect detection, J. High Energy Phys. 06 (2016) 152.
[8] M. Duerr, P. Fileviez Pérez, and J. Smirnov, Gamma-ray excess and the minimal dark matter model, J. High Energy Phys. 06 (2016) 008.
[9] D. Hooper, G. Krnjaic, A. J. Long, and S. D. Mcdermott, Can the inflaton also be a weakly interacting massive particle?, Phys. Rev. Lett. **122**, 091802 (2019).
[10] K. Fraser, A. Parikh, and W. L. Xu, A closer look at *CP*-violating Higgs portal dark matter as a candidate for the GCE, J. High Energy Phys. 03 (2021) 123.
[11] N. Aghanim *et al.* (Planck Collaboration), Planck 2018 results. VI. Cosmological parameters, Astron. Astrophys. **641**, A6 (2020); **652**, C4(E) (2021).
[12] J. M. Cline, P. Scott, K. Kainulainen, and C. Weniger, Update on scalar singlet dark matter, Phys. Rev. D **88**, 055025 (2013).
[13] J. A. Casas, D. G. Cerdeño, J. M. Moreno, and J. Quilis, Reopening the Higgs portal for single scalar dark matter, J. High Energy Phys. 05 (2017) 036.
[14] B. Díaz Sáez, J. Lahiri, and K. Möhling, Coscattering in the extended singlet-scalar Higgs portal, J. Cosmol. Astropart. Phys. 10 (2024) 001.
[15] P. De La Torre Luque, J. Smirnov, and T. Linden, Gamma-ray lines in 15 years of Fermi-LAT data: New constraints on Higgs portal dark matter, Phys. Rev. D **109**, L041301 (2024).
[16] A. Djouadi, O. Lebedev, Y. Mambrini, and J. Quevillon, Implications of LHC searches for Higgs–portal dark matter, Phys. Lett. B **709**, 65 (2012).
[17] G. Arcadi, A. Djouadi, and M. Raidal, Dark matter through the Higgs portal, Phys. Rep. **842**, 1 (2020).
[18] G. Krnjaic, Probing light thermal dark-matter with a Higgs portal mediator, Phys. Rev. D **94**, 073009 (2016).
[19] K. Ghorbani and H. Ghorbani, Scalar split WIMPs in future direct detection experiments, Phys. Rev. D **93**, 055012 (2016).
[20] J. Guo, Y. He, J. Liu, and X.-P. Wang, Heavy long-lived coannihilation partner from inelastic dark matter model and its signatures at the LHC, J. High Energy Phys. 04 (2022) 024.
[21] J. A. Casas, G. A. Gómez Vargas, J. M. Moreno, J. Quilis, and R. Ruiz de Austri, Extended Higgs-portal dark matter and the Fermi-LAT galactic center excess, J. Cosmol. Astropart. Phys. 06 (2018) 031.
[22] M. Ackermann *et al.* (Fermi-LAT Collaboration), The Fermi galactic center GeV excess and implications for dark matter, Astrophys. J. **840**, 43 (2017).
[23] A. McDaniel, M. Ajello, C. M. Karwin, M. Di Mauro, A. Drlica-Wagner, and M. A. Sánchez-Conde, Legacy analysis of dark matter annihilation from the Milky Way dwarf spheroidal galaxies with 14 years of Fermi-LAT data, Phys. Rev. D **109**, 063024 (2024).
[24] M. Di Mauro, M. Stref, and F. Calore, Investigating the effect of Milky Way dwarf spheroidal galaxies extension on dark matter searches with Fermi-LAT data, Phys. Rev. D **106**, 123032 (2022).
[25] A. Cuoco, M. Krämer, and M. Korsmeier, Novel dark matter constraints from antiprotons in light of AMS-02, Phys. Rev. Lett. **118**, 191102 (2017).
[26] G. Giesen, M. Boudaud, Y. Génolini, V. Poulin, M. Cirelli, P. Salati, and P. D. Serpico, AMS-02 antiprotons, at last! secondary astrophysical component and immediate implications for dark matter, J. Cosmol. Astropart. Phys. 09 (2015) 023.
[27] I. Cholis, T. Linden, and D. Hooper, A robust excess in the cosmic-ray antiproton spectrum: Implications for annihilating dark matter, Phys. Rev. D **99**, 103026 (2019).
[28] M. Trodden, Electroweak baryogenesis, Rev. Mod. Phys. **71**, 1463 (1999).
[29] G. W. Anderson and L. J. Hall, The electroweak phase transition and baryogenesis, Phys. Rev. D **45**, 2685 (1992).
[30] P. Huet and A. E. Nelson, Electroweak baryogenesis in supersymmetric models, Phys. Rev. D **53**, 4578 (1996).
[31] D. E. Morrissey and M. J. Ramsey-Musolf, Electroweak baryogenesis, New J. Phys. **14**, 125003 (2012).
[32] P. Athron, C. Balázs, A. Fowlie, L. Morris, and L. Wu, Cosmological phase transitions: From perturbative particle physics to gravitational waves, Prog. Part. Nucl. Phys. **135**, 104094 (2024).
[33] J. Aalbers *et al.* (LZ Collaboration), Dark matter search results from 4.2 tonne-years of exposure of the LUX-ZEPLIN (LZ) experiment, Phys. Rev. Lett. **135**, 011802 (2025).
[34] D. Tucker-Smith and N. Weiner, Inelastic dark matter, Phys. Rev. D **64**, 043502 (2001).
[35] R. J. Hill and M. P. Solon, Standard model anatomy of WIMP dark matter direct detection II: QCD analysis and hadronic matrix elements, Phys. Rev. D **91**, 043505 (2015).
[36] A. Alloul, N. D. Christensen, C. Degrande, C. Duhr, and B. Fuks, FeynRules 2.0—A complete toolbox for tree-level phenomenology, Comput. Phys. Commun. **185**, 2250 (2014).
[37] G. Belanger, F. Boudjema, A. Pukhov, and A. Semenov, MicrOMEGAs 2.0: A program to calculate the relic density of dark matter in a generic model, Comput. Phys. Commun. **176**, 367 (2007).
[38] J. Billard, L. Strigari, and E. Figueroa-Feliciano, Implication of neutrino backgrounds on the reach of next generation dark matter direct detection experiments, Phys. Rev. D **89**, 023524 (2014).

[39] P. Gondolo and G. Gelmini, Cosmic abundances of stable particles: Improved analysis, Nucl. Phys. **B360**, 145 (1991).
[40] G. Krnjaic, Freezing in, heating up, and freezing out: Predictive nonthermal dark matter and low-mass direct detection, J. High Energy Phys. 10 (2018) 136.
[41] A. Ghosh, A. Ibarra, T. Mondal, and B. Mukhopadhyaya, Gamma-ray signals from multicomponent scalar dark matter decays, J. Cosmol. Astropart. Phys. 01 (2020) 011.
[42] T. R. Slatyer, Energy injection and absorption in the cosmic dark ages, Phys. Rev. D **87**, 123513 (2013).
[43] T. R. Slatyer and C.-L. Wu, General constraints on dark matter decay from the cosmic microwave background, Phys. Rev. D **95**, 023010 (2017).
[44] L. Forestell, D. E. Morrissey, and G. White, Limits from BBN on light electromagnetic decays, J. High Energy Phys. 01 (2019) 074.
[45] P. F. Depta, M. Hufnagel, and K. Schmidt-Hoberg, Updated BBN constraints on electromagnetic decays of MeV-scale particles, J. Cosmol. Astropart. Phys. 04 (2021) 011.
[46] M. Baryakhtar, A. Berlin, H. Liu, and N. Weiner, Electromagnetic signals of inelastic dark matter scattering, J. High Energy Phys. 06 (2022) 047.
[47] M. Carrillo González and N. Toro, Cosmology and signals of light pseudo-Dirac dark matter, J. High Energy Phys. 04 (2022) 060.
[48] A. Berlin, G. Krnjaic, and E. Pinetti, Reviving MeV-GeV indirect detection with inelastic dark matter, Phys. Rev. D **110**, 035015 (2024).
[49] L. Goodenough and D. Hooper, Possible evidence for dark matter annihilation in the inner milky way from the Fermi Gamma Ray Space Telescope, arXiv:0910.2998.
[50] D. Hooper and L. Goodenough, Dark matter annihilation in the galactic center as seen by the Fermi Gamma Ray Space Telescope, Phys. Lett. B **697**, 412 (2011).
[51] D. Hooper and T. Linden, On the origin of the gamma rays from the galactic center, Phys. Rev. D **84**, 123005 (2011).
[52] K. N. Abazajian and M. Kaplinghat, Detection of a gamma-ray source in the galactic center consistent with extended emission from dark matter annihilation and concentrated astrophysical emission, Phys. Rev. D **86**, 083511 (2012); **87**, 129902(E) (2013).
[53] D. Hooper and T. R. Slatyer, Two emission mechanisms in the Fermi bubbles: A possible signal of annihilating dark matter, Phys. Dark Universe **2**, 118 (2013).
[54] C. Gordon and O. Macias, Dark matter and pulsar model constraints from galactic center Fermi-LAT gamma ray observations, Phys. Rev. D **88**, 083521 (2013); **89**, 049901 (E) (2014).
[55] T. Daylan, D. P. Finkbeiner, D. Hooper, T. Linden, S. K. N. Portillo, N. L. Rodd, and T. R. Slatyer, The characterization of the gamma-ray signal from the central milky way: A case for annihilating dark matter, Phys. Dark Universe **12**, 1 (2016).
[56] B. Zhou, Y.-F. Liang, X. Huang, X. Li, Y.-Z. Fan, L. Feng, and J. Chang, GeV excess in the Milky Way: The role of diffuse galactic gamma-ray emission templates, Phys. Rev. D **91**, 123010 (2015).
[57] F. Calore, I. Cholis, and C. Weniger, Background model systematics for the Fermi GeV excess, J. Cosmol. Astropart. Phys. 03 (2015) 038.
[58] M. Ajello *et al.* (Fermi-LAT Collaboration), Fermi-LAT observations of high-energy γ-ray emission toward the galactic center, Astrophys. J. **819**, 44 (2016).
[59] I. Cholis, Y.-M. Zhong, S. D. McDermott, and J. P. Surdutovich, Return of the templates: Revisiting the galactic center excess with multimessenger observations, Phys. Rev. D **105**, 103023 (2022).
[60] M. Di Mauro, Characteristics of the galactic center excess measured with 11 years of *Fermi*-LAT data, Phys. Rev. D **103**, 063029 (2021).
[61] D. Hooper, R. K. Leane, Y.-D. Tsai, S. Wegsman, and S. J. Witte, A systematic study of hidden sector dark matter: Application to the gamma-ray and antiproton excesses, J. High Energy Phys. 07 (2020) 163.
[62] M.-Y. Cui, Q. Yuan, Y.-L. S. Tsai, and Y.-Z. Fan, Possible dark matter annihilation signal in the AMS-02 antiproton data, Phys. Rev. Lett. **118**, 191101 (2017).
[63] A. Cuoco, J. Heisig, L. Klamt, M. Korsmeier, and M. Krämer, Scrutinizing the evidence for dark matter in cosmic-ray antiprotons, Phys. Rev. D **99**, 103014 (2019).
[64] J. M. Cline and K. Kainulainen, Electroweak baryogenesis and dark matter from a singlet Higgs, J. Cosmol. Astropart. Phys. 01 (2013) 012.
[65] V. Vaskonen, Electroweak baryogenesis and gravitational waves from a real scalar singlet, Phys. Rev. D **95**, 123515 (2017).
[66] B. Grzadkowski and D. Huang, Spontaneous *CP*-violating electroweak baryogenesis and dark matter from a complex singlet scalar, J. High Energy Phys. 08 (2018) 135.
[67] J. Ellis, M. Lewicki, M. Merchand, J. M. No, and M. Zych, The scalar singlet extension of the standard model: gravitational waves versus baryogenesis, J. High Energy Phys. 01 (2023) 093.
[68] S. Roy, Dark matter and electroweak baryogenesis with spontaneous *CP* violation in the early universe, Phys. Rev. D **113**, 055040 (2026).
[69] A. D. Linde, On the vacuum instability and the Higgs meson mass, Phys. Lett. **70B**, 306 (1977).
[70] A. D. Linde, Phase transitions in gauge theories and cosmology, Rep. Prog. Phys. **42**, 389 (1979).
[71] A. D. Linde, Decay of the false vacuum at finite temperature, Nucl. Phys. **B216**, 421 (1983); **B223**, 544(E) (1983).
[72] J. S. Langer, Statistical theory of the decay of metastable states, Ann. Phys. (N.Y.) **54**, 258 (1969).
[73] S. R. Coleman, The fate of the false vacuum. 1. Semiclassical theory, Phys. Rev. D **15**, 2929 (1977); **16**, 1248 (E) (1977).
[74] I. Affleck, Quantum statistical metastability, Phys. Rev. Lett. **46**, 388 (1981).
[75] A. Mazumdar and G. White, Review of cosmic phase transitions: Their significance and experimental signatures, Rep. Prog. Phys. **82**, 076901 (2019).
[76] M. Quiros, Finite temperature field theory and phase transitions, in *ICTP Summer School in High-Energy Physics and Cosmology* (1999), Vol. 1, pp. 187–259; arXiv:hep-ph/9901312.

[77] C. L. Wainwright, CosmoTransitions: Computing cosmological phase transition temperatures and bubble profiles with multiple fields, Comput. Phys. Commun. **183**, 2006 (2012).
[78] J. R. Espinosa, B. Gripaios, T. Konstandin, and F. Riva, Electroweak baryogenesis in non-minimal composite Higgs models, J. Cosmol. Astropart. Phys. 01 (2012) 012.
[79] S. Blasi and A. Mariotti, Domain walls seeding the electroweak phase transition, Phys. Rev. Lett. **129**, 261303 (2022).
[80] P. Agrawal, S. Blasi, A. Mariotti, and M. Nee, Electroweak phase transition with a double well done doubly well, J. High Energy Phys. 06 (2024) 089.
[81] P. Amaro-Seoane *et al.* (LISA Collaboration), Laser interferometer space antenna, arXiv:1702.00786.
[82] X. Gong *et al.*, Descope of the ALIA mission, J. Phys. Conf. Ser. **610**, 012011 (2015).
[83] W.-R. Hu and Y.-L. Wu, The Taiji program in space for gravitational wave physics and the nature of gravity, Natl. Sci. Rev. **4**, 685 (2017).
[84] V. Corbin and N. J. Cornish, Detecting the cosmic gravitational wave background with the big bang observer, Classical Quantum Gravity **23**, 2435 (2006).
[85] H. Kudoh, A. Taruya, T. Hiramatsu, and Y. Himemoto, Detecting a gravitational-wave background with next-generation space interferometers, Phys. Rev. D **73**, 064006 (2006).
[86] C. Caprini *et al.*, Science with the space-based interferometer eLISA. II: Gravitational waves from cosmological phase transitions, J. Cosmol. Astropart. Phys. 04 (2016) 001.
[87] S. Babak, A. Petiteau, and M. Hewitson, LISA sensitivity and SNR calculations, arXiv:2108.01167.
[88] T. L. Smith, T. L. Smith, R. R. Caldwell, and R. Caldwell, LISA for cosmologists: Calculating the signal-to-noise ratio for stochastic and deterministic sources, Phys. Rev. D **100**, 104055 (2019); **105**, 029902(E) (2022).
[89] M. Cepeda *et al.*, Report from Working Group 2: Higgs physics at the HL-LHC and HE-LHC, CERN Yellow Rep. Monogr. **7**, 221 (2019).
[90] I. Agapov *et al.*, Future circular lepton collider FCC-ee: Overview and status, in *Snowmass 2021* (2022), 3; arXiv:2203.08310.
[91] M. Benedikt *et al.*, Future circular hadron collider FCC-hh: Overview and status, arXiv:2203.07804.
[92] A. Aryshev *et al.* (ILC International Development Team Collaboration), The International Linear Collider: Report to snowmass 2021, arXiv:2203.07622.
[93] C. Accettura *et al.*, Towards a muon collider, Eur. Phys. J. C **83**, 864 (2023); **84**, 36(E) (2024).
[94] D. Curtin *et al.*, Exotic decays of the 125 GeV Higgs boson, Phys. Rev. D **90**, 075004 (2014).
[95] G. Aad *et al.* (ATLAS Collaboration), Search for invisible Higgs-boson decays in events with vector-boson fusion signatures using 139 fb^{-1} of proton-proton data recorded by the ATLAS experiment, J. High Energy Phys. 08 (2022) 104.
[96] A. Tumasyan *et al.* (CMS Collaboration), A search for decays of the Higgs boson to invisible particles in events with a top-antitop quark pair or a vector boson in proton-proton collisions at $\sqrt{s} = 13\mathrm{TeV}$, Eur. Phys. J. C **83**, 933 (2023).
[97] G. Aad *et al.* (ATLAS Collaboration), Combination of searches for invisible decays of the Higgs boson using 139 fb − 1 of proton-proton collision data at $s = 13\mathrm{TeV}$ collected with the ATLAS experiment, Phys. Lett. B **842**, 137963 (2023).
[98] L. Lee, C. Ohm, A. Soffer, and T.-T. Yu, Collider searches for long-lived particles beyond the standard model, Prog. Part. Nucl. Phys. **106**, 210 (2019); **122**, 103912(E) (2022).
[99] D. Curtin *et al.*, Long-lived particles at the energy frontier: The MATHUSLA physics case, Rep. Prog. Phys. **82**, 116201 (2019).
[100] M. Gon////çalves, M. Mühlleitner, R. Santos, and T. Trindade, Dark matter in multi-singlet extensions of the standard model, J. High Energy Phys. 03 (2026) 157.
[101] S. R. Coleman and E. J. Weinberg, Radiative corrections as the origin of spontaneous symmetry breaking, Phys. Rev. D **7**, 1888 (1973).
[102] S. P. Martin, Taming the Goldstone contributions to the effective potential, Phys. Rev. D **90**, 016013 (2014).
[103] J. Elias-Miro, J. R. Espinosa, and T. Konstandin, Taming infrared divergences in the effective potential, J. High Energy Phys. 08 (2014) 034.
[104] S. Baum, M. Carena, N. R. Shah, C. E. M. Wagner, and Y. Wang, Nucleation is more than critical: A case study of the electroweak phase transition in the NMSSM, J. High Energy Phys. 03 (2021) 055.
[105] A. Chatterjee, A. Datta, and S. Roy, Electroweak phase transition in the Z_3-invariant NMSSM: Implications of LHC and Dark matter searches and prospects of detecting the gravitational waves, J. High Energy Phys. 06 (2022) 108.
[106] P. Ghosh, T. Ghosh, and S. Roy, Interplay among gravitational waves, dark matter and collider signals in the singlet scalar extended type-II seesaw model, J. High Energy Phys. 10 (2023) 057.
[107] S. Roy, Dilution of dark matter relic abundance due to first order electroweak phase transition in the singlet scalar extended type-II seesaw model, Phys. Rev. D **111**, 015037 (2025).
[108] P. Bittar, S. Roy, and C. E. M. Wagner, Self consistent thermal resummation: A case study of the phase transition in 2HDM, J. High Energy Phys. 12 (2025) 021.
[109] L. Dolan and R. Jackiw, Symmetry behavior at finite temperature, Phys. Rev. D **9**, 3320 (1974).
[110] S. Weinberg, Gauge and global symmetries at high temperature, Phys. Rev. D **9**, 3357 (1974).
[111] D. A. Kirzhnits and A. D. Linde, Symmetry behavior in gauge theories, Ann. Phys. (N.Y.) **101**, 195 (1976).
[112] D. J. Gross, R. D. Pisarski, and L. G. Yaffe, QCD and instantons at finite temperature, Rev. Mod. Phys. **53**, 43 (1981).
[113] R. R. Parwani, Resummation in a hot scalar field theory, Phys. Rev. D **45**, 4695 (1992); **48**, 5965(E) (1993).
[114] P. B. Arnold and O. Espinosa, The effective potential and first order phase transitions: Beyond leading-order, Phys. Rev. D **47**, 3546 (1993); **50**, 6662(E) (1994).

[115] C. G. Boyd, D. E. Brahm, and S. D. H. Hsu, Resummation methods at finite temperature: The tadpole way, Phys. Rev. D **48**, 4963 (1993).
[116] B. Allen and J. D. Romano, Detecting a stochastic background of gravitational radiation: Signal processing strategies and sensitivities, Phys. Rev. D **59**, 102001 (1999).
[117] R.-G. Cai, Z. Cao, Z.-K. Guo, S.-J. Wang, and T. Yang, The gravitational-wave physics, Natl. Sci. Rev. **4**, 687 (2017).
[118] C. Caprini and D. G. Figueroa, Cosmological backgrounds of gravitational waves, Classical Quantum Gravity **35**, 163001 (2018).
[119] J. D. Romano and N. J. Cornish, Detection methods for stochastic gravitational-wave backgrounds: A unified treatment, Living Rev. Relativity **20**, 2 (2017).
[120] N. Christensen, Stochastic gravitational wave backgrounds, Rep. Prog. Phys. **82**, 016903 (2019).
[121] J. R. Espinosa, T. Konstandin, J. M. No, and G. Servant, Energy budget of cosmological first-order phase transitions, J. Cosmol. Astropart. Phys. 06 (2010) 028.
[122] M. S. Turner, E. J. Weinberg, and L. M. Widrow, Bubble nucleation in first order inflation and other cosmological phase transitions, Phys. Rev. D **46**, 2384 (1992).
[123] R. Apreda, M. Maggiore, A. Nicolis, and A. Riotto, Gravitational waves from electroweak phase transitions, Nucl. Phys. **B631**, 342 (2002).
[124] M. Hindmarsh, S. J. Huber, K. Rummukainen, and D. J. Weir, Numerical simulations of acoustically generated gravitational waves at a first order phase transition, Phys. Rev. D **92**, 123009 (2015).
[125] A. Kosowsky, M. S. Turner, and R. Watkins, Gravitational waves from first order cosmological phase transitions, Phys. Rev. Lett. **69**, 2026 (1992).
[126] A. Kosowsky, M. S. Turner, and R. Watkins, Gravitational radiation from colliding vacuum bubbles, Phys. Rev. D **45**, 4514 (1992).
[127] A. Kosowsky and M. S. Turner, Gravitational radiation from colliding vacuum bubbles: Envelope approximation to many bubble collisions, Phys. Rev. D **47**, 4372 (1993).
[128] C. Caprini *et al.*, Detecting gravitational waves from cosmological phase transitions with LISA: An update, J. Cosmol. Astropart. Phys. 03 (2020) 024.
[129] D. Bodeker and G. D. Moore, Electroweak bubble wall speed limit, J. Cosmol. Astropart. Phys. 05 (2017) 025.
[130] M. Hindmarsh, S. J. Huber, K. Rummukainen, and D. J. Weir, Gravitational waves from the sound of a first order phase transition, Phys. Rev. Lett. **112**, 041301 (2014).
[131] J. T. Giblin, Jr. and J. B. Mertens, Vacuum bubbles in the presence of a relativistic fluid, J. High Energy Phys. 12 (2013) 042.
[132] J. T. Giblin and J. B. Mertens, Gravitional radiation from first-order phase transitions in the presence of a fluid, Phys. Rev. D **90**, 023532 (2014).
[133] K. Schmitz, New sensitivity curves for gravitational-wave signals from cosmological phase transitions, J. High Energy Phys. 01 (2021) 097.
[134] C. Caprini and R. Durrer, Gravitational waves from stochastic relativistic sources: Primordial turbulence and magnetic fields, Phys. Rev. D **74**, 063521 (2006).
[135] T. Kahniashvili, A. Kosowsky, G. Gogoberidze, and Y. Maravin, Detectability of gravitational waves from phase transitions, Phys. Rev. D **78**, 043003 (2008).
[136] T. Kahniashvili, L. Campanelli, G. Gogoberidze, Y. Maravin, and B. Ratra, Gravitational radiation from primordial helical inverse cascade MHD turbulence, Phys. Rev. D **78**, 123006 (2008); **79**, 109901(E) (2009).
[137] T. Kahniashvili, L. Kisslinger, and T. Stevens, Gravitational radiation generated by magnetic fields in cosmological phase transitions, Phys. Rev. D **81**, 023004 (2010).
[138] C. Caprini, R. Durrer, and G. Servant, The stochastic gravitational wave background from turbulence and magnetic fields generated by a first-order phase transition, J. Cosmol. Astropart. Phys. 12 (2009) 024.
[139] L. Kisslinger and T. Kahniashvili, Polarized gravitational waves from cosmological phase transitions, Phys. Rev. D **92**, 043006 (2015).
[140] M. Hindmarsh and M. Hijazi, Gravitational waves from first order cosmological phase transitions in the sound shell model, J. Cosmol. Astropart. Phys. 12 (2019) 062.
[141] H.-K. Guo, K. Sinha, D. Vagie, and G. White, Phase transitions in an expanding universe: Stochastic gravitational waves in standard and non-standard histories, J. Cosmol. Astropart. Phys. 01 (2021) 001.
[142] M. B. Hindmarsh, M. Lüben, J. Lumma, and M. Pauly, Phase transitions in the early universe, SciPost Phys. Lect. Notes **24**, 1 (2021).
[143] U.-L. Pen and N. Turok, Shocks in the early universe, Phys. Rev. Lett. **117**, 131301 (2016).
[144] M. Hindmarsh, S. J. Huber, K. Rummukainen, and D. J. Weir, Shape of the acoustic gravitational wave power spectrum from a first order phase transition, Phys. Rev. D **96**, 103520 (2017); **101**, 089902(E) (2020).
[145] D. J. Weir, Gravitational waves from a first order electroweak phase transition: A brief review, Phil. Trans. R. Soc. A **376**, 20170126 (2018); **381**, 20230212(E) (2023).